minerals

MDPI

Article

Strongly Peraluminous Highly Fractionated I-Type Granite from Bangong–Nujiang Metallogenic Belt, Tibet: Implications for Continental Evolution and Evaluation of Economic Potentiality

Nan Wang [1], Zhibo Liu [1,*] and Min Lei [2,*]

[1] MNR Key Laboratory of Metallogeny and Mineral Assessment, Institute of Mineral Resources, Chinese Academy of Geological Sciences, Beijing 100037, China; wangnan_0912@sina.com
[2] Institute of Geology, Chinese Academy of Geological Sciences, Beijing 100037, China
* Correspondence: geoleo@163.com (Z.L.); leiminlm@126.com (M.L.)

Abstract: The research on highly fractionated granite has significant implications for both the evolution and compositional maturation of the continental crust and metallogenic exploration. As a means of further understanding crustal evolution and promoting ore exploration in the Bangong–Nujiang metallogenic belt (BNMB), we present the petrography, zircon LA–ICP–MS U–Pb age, and Hf isotopic data, along with the whole-rock geochemical and Sr–Nd isotopic composition on Kese highly fractionated granite in the Baingoin area within the BNMB, central Tibet. The results show that Kese granite possesses a zircon U–Pb age of 127.8 ± 1.7 Ma and a relative enrichment in zircon Hf isotopic composition (−12.8~+0.3) with a two-stage Hf model age of 1.2~2.0 Ga. This granite belongs to the high-K calc-alkaline series, characterized by a strongly peraluminous feature, and is enriched in large-ion lithophile elements (LILEs) and Nd isotopes (−7.86~−7.74). The granite was likely to have been derived from the mixed melts derived from 40%~45% juvenile basaltic lower crust, 15%~20% ancient lower, and 40% middle–upper, following intense fractional crystallization processes involving amphibole, biotite, plagioclase, and some accessory minerals during the magma's evolution. We infer that Kese highly fractionated granite can be formed from the continental collision of the Lhasa–Qiangtang terranes initiated before 128 Ma. The reworking of pre-existing juvenile and ancient crustal materials drove the composition of the northern Lhasa terrane to that of a mature continental crust. Moreover, the distinctive geochemical features have shown that the high degree of differentiation led to intense magmatic–hydrothermal interaction during the formation of Kese granite. A comparison of the geochemical characteristics of mineralized and barren granites suggests that the highly fractionated granites in Baingoin from the BNMB have a high economic potential and are suitable for preliminary exploration of Sn–W-(U) deposits.

Keywords: economic potentiality; reworking of continental crust; petrogenesis; highly fractionated granite; Bangong–Nujiang metallogenic belt

Citation: Wang, N.; Liu, Z.; Lei, M. Strongly Peraluminous Highly Fractionated I-Type Granite from Bangong–Nujiang Metallogenic Belt, Tibet: Implications for Continental Evolution and Evaluation of Economic Potentiality. *Minerals* **2023**, *13*, 1152. https://doi.org/10.3390/min13091152

Academic Editor: Jaroslav Dostal

Received: 23 July 2023
Revised: 17 August 2023
Accepted: 28 August 2023
Published: 30 August 2023

1. Introduction

Highly fractionated granites are similar in geochemical properties to mature continental crusts and have been considered to be an excellent window into the processes of compositional evolution of the continental crust [1,2]. Meanwhile, fractional crystallization during magma's evolution facilitates the enrichment of W–Sn–Nb–Ta in magma [3,4]; thus, highly fractionated granites usually possess mineralized specialization [5,6]. Research has shown that numerous deposits are thought to have genetic links with highly fractionated granite, such as some W–Sn–Nb–Ta, REE, and Li–Be deposits in south China, southern Tibet, and the Variscan orogeny [7–10]. Therefore, recognition and research of highly fractionated granites can also provide direct evidence for the exploration and economic potentiality evaluation of genetically related mineral deposits.

Since the Paleozoic era, the Tibetan Plateau has undergone complex growth and evolution due to the amalgamation of terranes over several orogenic cycles. It has the thickest continental crust in the world and provides favorable metallogenic conditions for the formation of large deposits [11–14]. The Mesozoic Bangong–Nujiang suture zone (BNSZ) in central Tibet, as the youngest suture zone before the India–Asian collision, records the evolution of the Bangong–Nujiang Tethyan Ocean (BNTO) from its opening to its closure, along with the addition of the Lhasa terrane at the southern margin of Asia [15,16]. In the last decade, extensive research has been conducted on the continental crust evolution and ore deposits caused by the evolution of the BNTO and collision of adjacent terranes (Lhasa–Qiangtang) during the late Early Cretaceous and Late Cretaceous periods [17–21], and an idea of Bangong–Nujiang metallogenic belt (BNMB) has been proposed [22]. Previous research indicates that the north Lhasa terrane underwent simultaneous growth and reworking of crust [23,24], and the formed ore deposits are mainly Cu–Au–Mo deposits in this period (such as a ~120 Ma Duolong Cu–Au deposit, ~118 Ma Jinmuguo Mo polymetallic deposit, 117–112 Ma Shesuo–Xiongmei Cu mineralized zone, ~88 Ma Gaerqiong–Galale Cu–Au deposit, and ~83 Ma Sangri Cu–Mo deposit) [25–30]. However, less research has been conducted on the crustal evolution process during the middle Early Cretaceous. Furthermore, it is also necessary to determine the tectonic background that caused the crustal evolution and whether such crustal evolution provides the possibility for the mineralization of any mineral species.

During the regional geological survey, the authors discovered several highly fractionated granites in the Baingoin area, in the northern Lhasa terrane. The ages of these granitoids differ from those reported for highly fractionated granitoids in BNMB [31–33]. In this study, U–Pb chronological and Hf isotopic data of zircon, whole-rock geochemistry, and Rb–Sr–Sm–Nd isotopic data are presented for Kese highly fractionated granite within the BNMB. This study aims to provide further information regarding the genesis type and evolution of magma and the evolution of the continental crust, evaluate the ore-bearing potentiality, and provide crucial clues for further mineral prospecting.

2. Geological Setting and Petrography

2.1. Geological Setting

The Tibetan Plateau is divided into several terranes. Among these are Qaidam, Songpan–Ganzi, Qiangtang, Lhasa, and Himalaya terranes from north to south. Interposing sutures separate them, including Ayimaqin–Kunlun Mutztagh, Jinshajiang, Bangong–Nujiang, and Indus–Yarlung sutures [11,12]. The BNSZ extends over two thousand kilometers and is dominated by Jurassic–Cretaceous flysch, volcanic rocks, and mélange, accompanied by rare but widely scattered ophiolitic fragments of the Mesozoic BNTO [34]. The Lhasa terrane is located south of the BNSZ and can be divided into northern, central, and southern Lhasa terranes (NL, CL, and CL) [18].

Located between the Shiquanhe–Nam Tso mélange and BNSZ, the northern Lhasa terrane comprises Jurassic sandstone with interbedded volcanic rocks (Jienu group), flysh formation (Lagongtang formation), and limestone (Rila formation), Early Cretaceous volcano–sedimentary rocks (Qushenla and Duoni formation), limestone (Langshan group), and Late Cretaceous Molasse formation (Jingzhushan formation). It has also been found that several intermediate–felsic igneous rocks have developed in the northern Lhasa terrane, the majority of which have been emplaced in the Cretaceous [18,23,34–36]. Regional structures are mainly NW–SE trending, and most faults are thrust faults, which determine the distribution direction of the strata and intrusion.

2.2. Petrography of Kese Granite

Kese granite is located in the NNW direction of Baingoin County and outcrops as a stock (Figures 1 and 2a). Previous studies proposed that the Kese granite belonged to fine-grained mica-monzogranite or granodiorite [35]. However, the field investigation revealed that the Kese granite primarily comprises granite and overlaps with Diqian granodiorite

without a clearly defined boundary (Figure 2a). Based on the zircon U–Pb dating results, we infer that Kese granite was formed later than Diqian granodiorite (~134.4 Ma) [37].

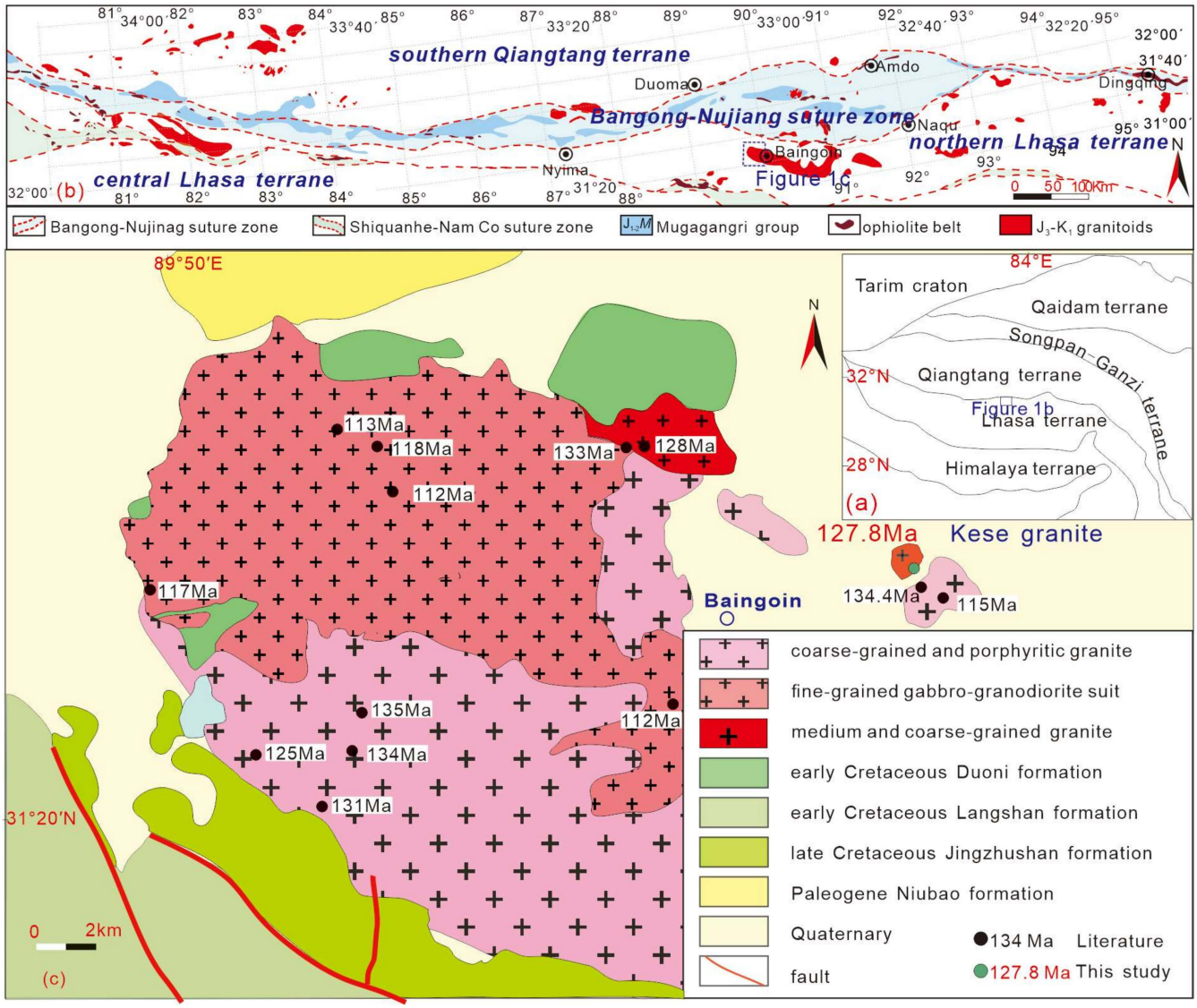

Figure 1. Geological sketch map of Tibetan Plateau (**a**), distribution of late Jurassic–early Cretaceous granites of BNMB (**b**) and geological sketch map of Baingoin area, central Tibet. ((**a**) modified after [34]; (**b**) modified after [23]; (**c**) age data from [23,35,37–40]).

These samples of Kese granite are mostly granitic in component, with yellow or red colors and medium-grained textures. Among the minerals, the dominant ones are K-feldspar (~48%), quartz (30%), and plagioclase (20%), while biotite and muscovite are minor (~2%) (Figure 2c), with accessory minerals such as sphene, zircon, apatite, and Fe–Ti oxides. Some K-feldspars show obvious metasomatic and secondary characteristics. Plagioclase is localized and sericitized.

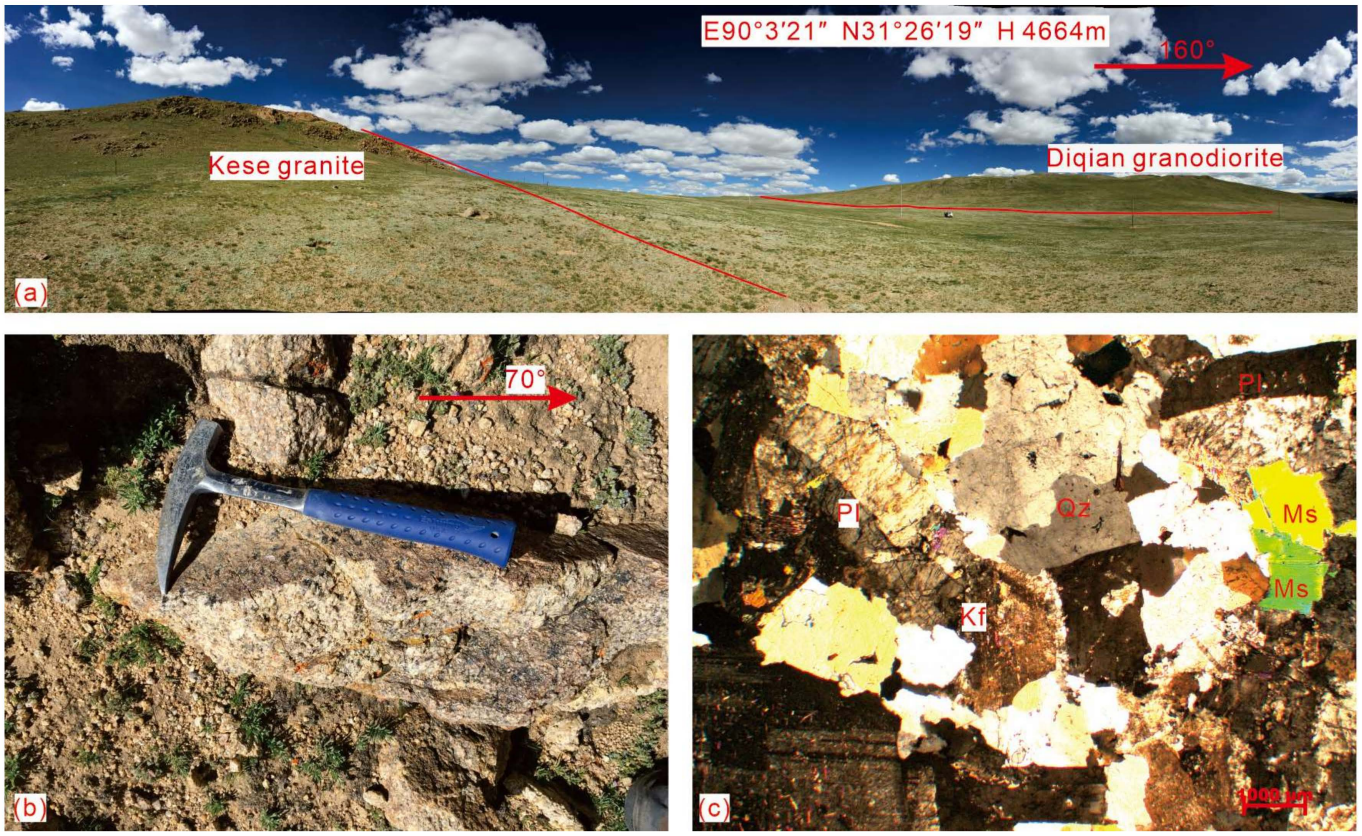

Figure 2. Outcrops and photomicrographs of Kese granite in BNMB, central Tibet. ((**a**,**b**) Outcrops of Kese granite; (**c**) photomicrographs of Kese granite, consisting of Kf, Pl, Qz, Bt, and Ms).

3. Analytical Methods

3.1. Zircon U–Pb Dating

A laser ablation inductively coupled plasma mass spectrometry (LA–ICP–MS) method was used to conduct the U, Th, and Pb analysis of zircons at the Institute of Geology, Chinese Academy of Geological Sciences, as described in the work by [41]. The spot sizes were ~32 μm, and data were calibrated according to the M127 reference zircon. GJ-1 zircon (599.8 ± 1.7 Ma, 2σ) [42] and plesovice zircon (337.13 ± 0.37 Ma, 2σ) [43] were selected as the reference standards, and every five unknowns were analyzed with the standard zircon first. Using the ICPMSDataCal programs, data processing was performed [44]. Due to the influence of common lead in inclusions, most analyses with $^{206}Pb/^{204}Pb$ values larger than 1000 had the ^{204}Pb measured not corrected for the common lead component. A summary of the analytical data is presented in Table 1 and represented graphically as concordia diagrams with a 1σ error. Using Isoplot at 95% confidence levels, the ages were calculated as weighted means with two standard deviations each [45].

3.2. Whole-Rock Geochemistry

A tungsten carbide shatter box was used to prepare whole-rock powders for eleven samples. At the National Research Center for Geoanalysis, Chinese Academy of Geological Sciences, the concentrations of major, trace, and rare earth elements (REEs) in the whole rock were determined using X-ray fluorescence (XRF) and inductively coupled plasma mass spectrometry (ICP–MS). The XRF method analyzed the major elements with analytical uncertainties <5%. Analysis of trace and REEs was performed using ICP–MS, and cations exchange analysis was used to separate REEs. As a result, there were around 5% analytical uncertainties for elements with abundances less than 10 ppm and about 10% for those with abundances greater than 10 ppm.

Table 1. LA–ICP–MS zircon U–Pb isotopic analyses for the samples of Kese granite in Baingoin area, central Tibet.

Spot	Concentrations (ppm)				Isotopic Ratios						Isotopic Ages (Ma)					
	Pb	Th	U	Th/U	$^{207}Pb/^{206}Pb$	1σ	$^{207}Pb/^{235}U$	1σ	$^{206}Pb/^{238}U$	1σ	$^{207}Pb/^{206}Pb$	1σ	$^{207}Pb/^{235}U$	1σ	$^{206}Pb/^{238}U$	1σ
D17R23_1	9.17	84	944	0.09	0.05035	0.00083	0.14082	0.00247	0.02039	0.00025	211.1	37.8	133.8	2.2	130.1	1.6
D17R23_2	3.85	44	406	0.11	0.04994	0.00115	0.13662	0.00324	0.02009	0.00027	192.4	52.7	130.0	2.9	128.2	1.7
D17R23_3	14.16	90	1585	0.06	0.05005	0.00078	0.1342	0.00224	0.01885	0.00023	197.4	35.9	127.9	2.0	120.4	1.5
D17R23_4	11.97	72	1298	0.06	0.04902	0.00077	0.13539	0.00227	0.01989	0.00024	149.0	36.3	128.9	2.0	127.0	1.5
D17R23_5	20.17	101	2056	0.05	0.05035	0.00068	0.14441	0.00213	0.02058	0.00025	211.3	31.1	137.0	1.9	131.3	1.6
D17R23_6	20.19	119	1932	0.06	0.05693	0.00077	0.15365	0.00226	0.0194	0.00023	488.1	29.9	145.1	2.0	123.8	1.5
D17R23_7	7.91	69	846	0.08	0.04874	0.00087	0.13628	0.00257	0.02024	0.00025	135.5	41.4	129.7	2.3	129.2	1.6
D17R23_8	3.71	81	376	0.22	0.04939	0.00118	0.14281	0.00352	0.02109	0.00028	166.2	54.9	135.5	3.1	134.6	1.8
D17R23_9	7.44	65	793	0.08	0.04943	0.00086	0.13974	0.00257	0.02006	0.00025	168.3	40.2	132.8	2.3	128.0	1.6
D17R23_10	16.75	70	1797	0.04	0.04925	0.0007	0.13726	0.00211	0.02	0.00024	159.6	32.8	130.6	1.9	127.6	1.5
D17R23_11	5.81	65	614	0.11	0.04893	0.00096	0.13774	0.00284	0.02045	0.00026	144.3	45.5	131.0	2.5	130.5	1.7
D17R23_12	8.38	60	868	0.07	0.05177	0.00086	0.14164	0.0025	0.01969	0.00024	275.2	37.7	134.5	2.2	125.7	1.5
D17R23_13	2.42	88	268	0.33	0.04716	0.00137	0.13838	0.00409	0.02026	0.00029	56.7	68.1	131.6	3.7	129.3	1.8
D17R23_14	9.84	113	1069	0.11	0.05044	0.00089	0.13703	0.00255	0.01927	0.00024	215.1	40.3	130.4	2.3	123.0	1.5
D17R23_15	118.03	64	372	0.17	0.12797	0.0014	4.6463	0.06444	0.26144	0.0031	2070.3	19.2	1757.6	11.6	1497.2	15.8
D17R23_16	8.84	59	912	0.07	0.05169	0.00089	0.14305	0.0026	0.0198	0.00025	271.9	38.8	135.8	2.3	126.4	1.6
D17R23_17	14.49	89	1582	0.06	0.04936	0.00072	0.13325	0.0021	0.0196	0.00024	164.9	33.8	127.0	1.9	125.1	1.5
D17R23_18	9.94	75	1024	0.07	0.04992	0.00087	0.14357	0.00266	0.02056	0.00026	191.2	40.2	136.2	2.4	131.2	1.6
D17R23_19	3.43	92	357	0.26	0.04883	0.00115	0.13971	0.00338	0.02079	0.00028	139.4	54.2	132.8	3.0	132.6	1.8
D17R23_20	1083.99	552	1336	0.41	0.18092	0.00188	11.51627	0.14278	0.47356	0.00556	2661.4	17.1	2565.9	11.6	2499.1	24.3
D17R23_21	9.90	73	1032	0.07	0.04958	0.0008	0.14031	0.00242	0.02043	0.00025	175.4	37.4	133.3	2.2	130.4	1.6
D17R23_22	18.32	217	243	0.89	0.06557	0.00091	1.09511	0.01859	0.12147	0.00148	792.8	28.9	751.0	9.0	739.0	8.5

3.3. Zircon Hf Isotopic Analyses

At the Institute of Geology, Chinese Academy of Geological Sciences, zircon Hf isotope analysis was conducted in situ with a GeoLasPro 193 nm laser ablation microprobe coupled to a Neptune multi-collector ICP–MS. Detailed descriptions of the instrumental conditions and the data acquisition procedure were provided by [46]. Depending on the size of the ablated domains, a stationary spot was used with a beam diameter of 44 mm. Helium was used as a carrier gas to transport the ablated sample from the laser ablation cell to the ICP–MS torch via a mixing chamber that contained argon. In order to correct the isobaric interferences of ^{176}Lu and ^{176}Yb on ^{176}Hf, the ratios $^{176}Yb/^{173}Yb = 0.796218$ and $^{176}Lu/^{175}Lu = 0.02658$ were determined [47]. In order to correct for instrumental mass bias, the Hf and Yb isotope ratios were normalized to a $^{179}Hf/^{177}Hf$ ratio of 0.7325 and a $^{172}Yb/^{173}Yb$ ratio of 1.35274, respectively [47]. The mass bias behavior of Lu was assumed to follow that of Yb; the mass bias correction protocol details are described in the work of [46]. As a reference standard, zircon GJ1 had a weighted average $^{176}Hf/^{177}Hf$ ratio of 0.282007 ± 0.000007 (2σ, $n = 36$). The calculated Hf single-stage (t_{DM}) and two-stage model age (t_{DMC}) were based on a depleted mantle source with a present-day $^{176}Hf/^{177}Hf$ ratio of 0.28325 and a ^{176}Lu decay constant of $1.865 \times 10^{-11} a^{-1}$ [48] and a mean $^{176}Lu/^{177}Hf$ value of 0.015 for the average continental crust [49].

3.4. Sr–Nd Isotopic Analyses

Measurements of Sr and Nd isotopes were carried out at Beijing Createch Testing Technology Company, Beijing, China. In a clean laboratory of 1000, all chemical preparations were performed on class 100 work benches. A SavillexTM PFA screw-top beaker was filled with about 150 mg of sample powder. Samples were prepared by adding concentrated HNO_3 and HF (1 mL and 2 mL) and heating the sealed beakers on a hotplate at 150 °C for a week. After digestion, acids were evaporated on the hotplate, and residues were dissolved in 1 mL of concentrated HCl. There were then three repetitions of this procedure. After that, the samples were dissolved in 1.5 mL of either 3.5 M HNO_3 or 3 M HCl for Sr or Nd purification, respectively.

Separation and purification of Sr was carried out using Sr-Spec (Triskem, 100–150 μm) resin. As a first step in the Nd purification process, REEs were rinsed with 6 M HCl using cation exchange resins (AG50W-X12, 200–400 mesh). Then, Nd was separately purified from REEs by 0.25 M using LN resins (Triskem, 100–150 μm). Analysis of Sr and Nd isotopic compositions was conducted using a Thermo Fisher Scientific Neptune Plus MC–ICP–MS. By applying the exponential fractionation law and assuming $^{88}Sr/^{86}Sr = 8.375209$ and $^{146}Nd/^{144}Nd = 0.7219$, $^{87}Sr/^{86}Sr$ and $^{143}Nd/^{144}Nd$ ratios were corrected for instrumental mass fractionation. Based on [50], modifications were made to this method.

For accuracy monitoring, NBS 987 was repeatedly tested, yielding an average $^{87}Sr/^{86}Sr$ value of 0.710249 ± 13 (2SD, n = 15). At the same time, the in-house standard GSB Nd was used to assess the stability of $^{143}Nd/^{144}Nd$, yielding a result of 0.512195 ± 6 (2SD, n = 9). In international basalt standards, BCR-2 and BHVO-2,$^{143}Nd/^{144}Nd$ results were 0.512620 ± 0.000003 and 0.512968 ± 0.000004, respectively.

4. Results

4.1. Zircon U–Pb Geochronology

One sample was selected from Kese granite (D17R23) for zircon LA–ICP–MS U–Pb geochronological and Lu–Hf isotopic analysis. The data and cathodoluminescence (CL) image and U–Pb concordia plot of representative zircon grains are shown in Table 1 and Figure 3, respectively.

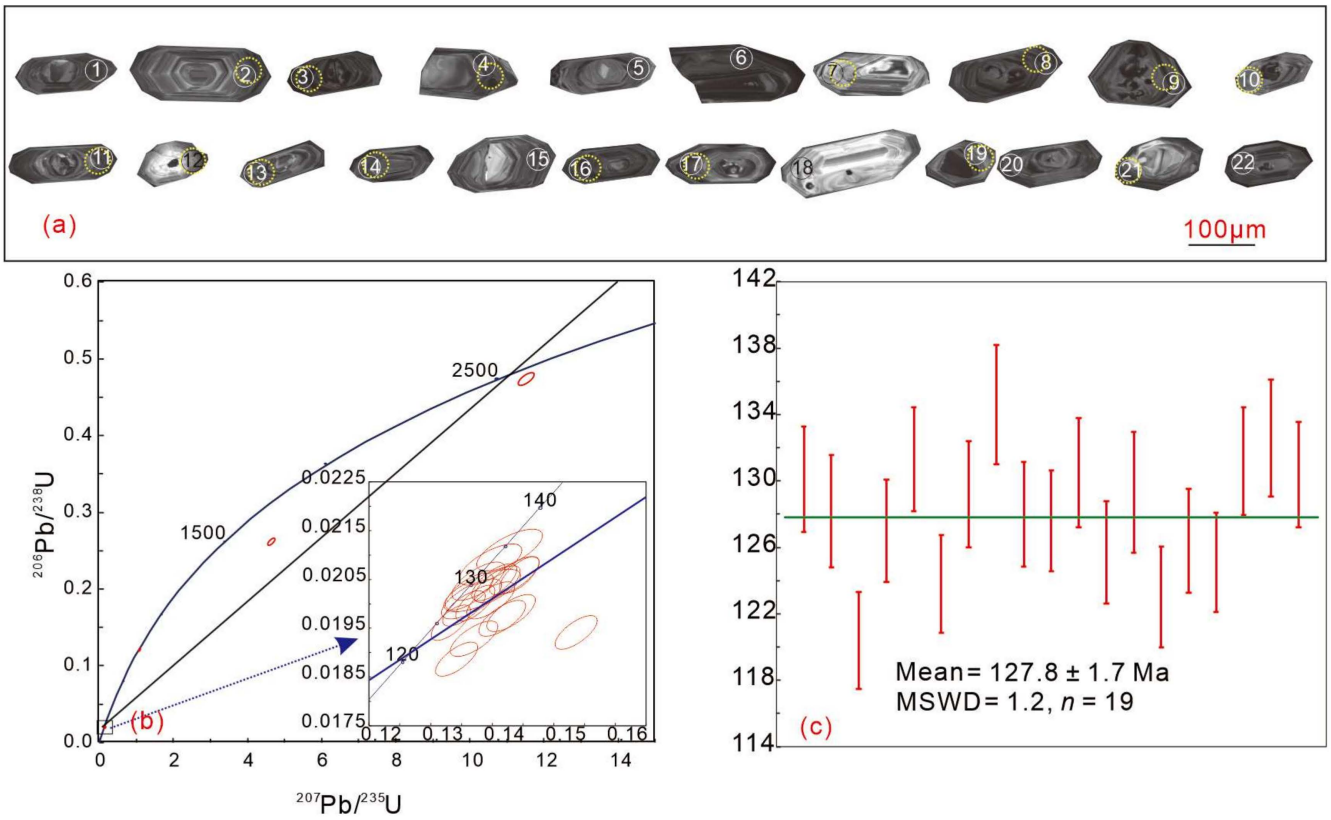

Figure 3. Cathodoluminescence (CL) images ((**a**), solid and dashed circles indicate the locations of LA–ICP–MS U–Pb and Hf analyses, respectively), U–Pb concordia; (**b**) weighted average age plots; (**c**) of zircon grains from Kese granite in BNMB, central Tibet.

In Kese granite, all zircon grains were off-white, having euhedral, stubby, or long prismatic forms with a length of 80~200 μm. They had a common aspect ratio of 1.5 to 2. As can be seen in CL images, the zircons exhibit oscillatory zoning, which is typical of magmatic zircons, whereas the bright CL images suggest that the U, Th, and REE contents are relatively low [51]. A Th/U average ratio of 0.16 was found in zircons from the sample, with Th contents ranging from 44 to 542 ppm and U contents ranging from 243 to 2056 ppm, suggesting a magmatic origin [52]. The $^{206}Pb/^{238}U$ ages from nineteen zircons are consistent, with a weighted mean age of 127.8 ± 1.7 Ma (MSWD = 1.2) (Figure 3b). It is worth pointing out that deviated ages were not considered in analysis locations 15, 20, and 22, indicative of captured zircon grains from Proterozoic materials according to the CL images.

4.2. Whole-Rock Geochemistry

Table 2 shows the concentrations of major and trace elements. Geochemically, Kese granite samples have uniform compositions and show high SiO_2 (74.86~77.42 wt%), Al_2O_3 (12.71~13.84 wt%), and K_2O contents (4.15~4.98 wt%), but low $Fe_2O_3{}^T$ (0.68~2.06 wt%) and CaO contents (0.28~0.97 wt%), and an accordingly high K_2O/Na_2O (1.41~1.95) ratio and $Na_2O + K_2O$ content (7.09~7.61 wt%), which indicates that these granites are classified as granite with and high-K calc-alkaline series features (Figure 4). The A/CNK ($Al_2O_3/(CaO + Na_2O + K_2O)$ molar ratios) range from 1.19 to 1.32, reflecting strongly peraluminous properties (Figure 5). Generally, these samples exhibit high Si, K, and total alkaline contents and lower Mg, Fe, and Ca contents.

Table 2. Whole-rock major (wt%) and trace elements (ppm) analysis of Kese granite in Baingoin area, central Tibet.

Sample No.	D16R15	D16R23	D17R12	D17R15	D17R22	D17R24	D17R26	D17R27	D17R28
SiO_2	74.86	76.66	75.05	76.13	77.42	77.20	76.48	76.58	76.50
TiO_2	0.14	0.14	0.13	0.12	0.11	0.09	0.13	0.10	0.10
Al_2O_3	13.84	12.76	13.35	13.15	12.96	12.90	13.36	12.71	12.88
TFe_2O_3	1.32	1.56	1.57	1.53	0.73	0.68	0.94	2.06	1.77
MnO	0.03	0.04	0.04	0.04	0.02	0.01	0.02	0.04	0.03
MgO	0.24	0.20	0.18	0.18	0.13	0.05	0.17	0.15	0.17
CaO	0.97	0.59	0.62	0.56	0.43	0.34	0.32	0.46	0.28
Na_2O	2.89	2.59	2.85	2.73	2.94	2.85	2.55	2.94	2.49
K_2O	4.72	4.87	4.59	4.87	4.30	4.62	4.98	4.15	4.78
P_2O_5	0.11	0.17	0.17	0.17	0.14	0.14	0.19	0.18	0.16
LOI	0.65	0.63	0.93	0.77	0.80	0.83	0.89	0.69	0.88
Total	99.66	100.21	99.36	100.15	99.98	99.71	100.03	99.98	99.98
A/CNK	1.19	1.20	1.24	1.22	1.26	1.25	1.31	1.25	1.32
C/NK	1.40	1.34	1.38	1.35	1.37	1.33	1.39	1.36	1.39
Ga	17.6	16.8	18.7	17.9	16.9	16.4	17.6	15.7	16.5
Rb	386	441	499	497	446	436	462	440	417
Sr	79.6	32.7	34.7	32.2	28.1	29.3	23.0	31.9	32.0
Y	19.0	24.3	22.8	21.3	21.2	20.8	23.2	21.9	17.7
Zr	74.0	63.0	62.0	69.0	55.0	60.0	60.0	75.0	52.0
Nb	10.5	11.8	14.7	13.2	10.8	10.4	12.7	12.6	9.2
Ba	262.0	74.1	76.4	73.3	62.1	67.5	63.0	65.6	77.8
Hf	2.2	2.1	2.0	2.2	2.0	2.1	2.1	2.5	1.7
Ta	1.9	2.6	3.5	3.6	3.0	2.6	3.8	3.7	2.7
Pb	32.1	26.7	24.3	25.6	28.0	22.8	24.1	28.6	25.0
Bi	0.29	1.99	1.76	2.26	1.55	1.07	1.35	1.66	1.05
Th	8.88	8.35	8.11	7.99	7.99	7.86	8.05	8.40	7.42
U	3.16	3.29	5.06	4.05	2.84	2.56	2.95	3.50	1.88
Li	60.6	109.5	170.0	144.5	80.6	72.8	69.7	69.9	46.5
Be	0.91	1.45	0.54	0.91	1.50	1.46	1.15	1.56	1.31
Sc	5.2	5.1	5.5	4.5	4.3	3.8	4.7	3.5	4.2
V	8	8	17	13	6	6	5	6	7
Cr	30	13	21	14	32	14	19	31	33
Co	1.3	1.7	0.6	0.9	0.5	0.7	0.8	0.8	0.8
Ni	2.4	2.0	1.6	1.7	1.1	1.1	1.2	2.0	2.6
Cu	2.3	8.0	20.0	19.8	4.8	2.8	0.2	14.5	12.7
Zn	31	29	39	30	12	11	19	18	19
Cs	24.9	48.8	48.2	51.5	32.3	29.5	33.4	36.5	21.0
La	15.7	12.1	10.8	10.7	9.5	9.4	10.2	10.2	8.8

Table 2. *Cont.*

Sample No.	D16R15	D16R23	D17R12	D17R15	D17R22	D17R24	D17R26	D17R27	D17R28
Ce	31.9	27.5	24.6	23.1	21.8	19.9	23.3	21.5	19.0
Pr	3.52	2.51	2.75	2.72	2.20	2.15	2.36	2.63	2.30
Nd	12.0	9.3	10.7	9.9	8.0	7.9	8.8	9.1	8.1
Sm	3.05	2.61	2.61	2.66	2.33	2.27	2.50	2.43	2.23
Eu	0.50	0.26	0.26	0.28	0.21	0.22	0.21	0.25	0.25
Gd	2.80	3.19	3.03	2.98	2.75	2.77	2.87	2.95	2.36
Tb	0.52	0.64	0.61	0.59	0.53	0.53	0.57	0.60	0.50
Dy	3.17	4.00	3.70	3.58	3.60	3.49	3.92	3.91	3.13
Ho	0.61	0.78	0.68	0.70	0.68	0.67	0.74	0.76	0.59
Er	1.81	2.26	2.01	2.00	2.08	1.98	2.25	2.18	1.75
Tm	0.28	0.34	0.30	0.29	0.30	0.28	0.33	0.36	0.25
Yb	1.94	2.30	1.90	1.94	2.16	2.01	2.24	2.33	1.71
Lu	0.29	0.36	0.27	0.28	0.31	0.29	0.33	0.36	0.25
∑REE	78.09	68.15	64.22	61.72	56.45	53.86	60.62	59.56	51.22
$(La/Yb)_N$	5.80	3.77	4.08	3.96	3.15	3.35	3.27	3.14	3.69
Sr/Y	4.19	1.35	1.52	1.51	1.33	1.41	0.99	1.46	1.81
Eu/Eu*	0.52	0.28	0.28	0.30	0.25	0.27	0.24	0.29	0.33
DI	90.4	92.7	91.8	92.5	94.1	94.9	93.9	92.4	93.1
Tzr (oC)	739	729	728	736	722	729	731	745	721
Sr–Nd isotope data									
$^{87}Rb/^{86}Sr$			41.5018	44.5448					
$^{87}Sr/^{86}Sr$			0.800659	0.789813					
$^{147}Sm/^{144}Nd$			0.1476	0.1626					
$^{143}Nd/^{144}Nd$			0.512200	0.512207					
$(^{87}Rb/^{86}Sr)_i$			0.7253	0.7089					
$(^{143}Nd/^{144}Nd)_i$			0.5121	0.5121					
$\varepsilon_{Nd}(t)$			−7.74	−7.86					
t_{DM1}			2180	2795					
t_{DM2}			1545	1552					

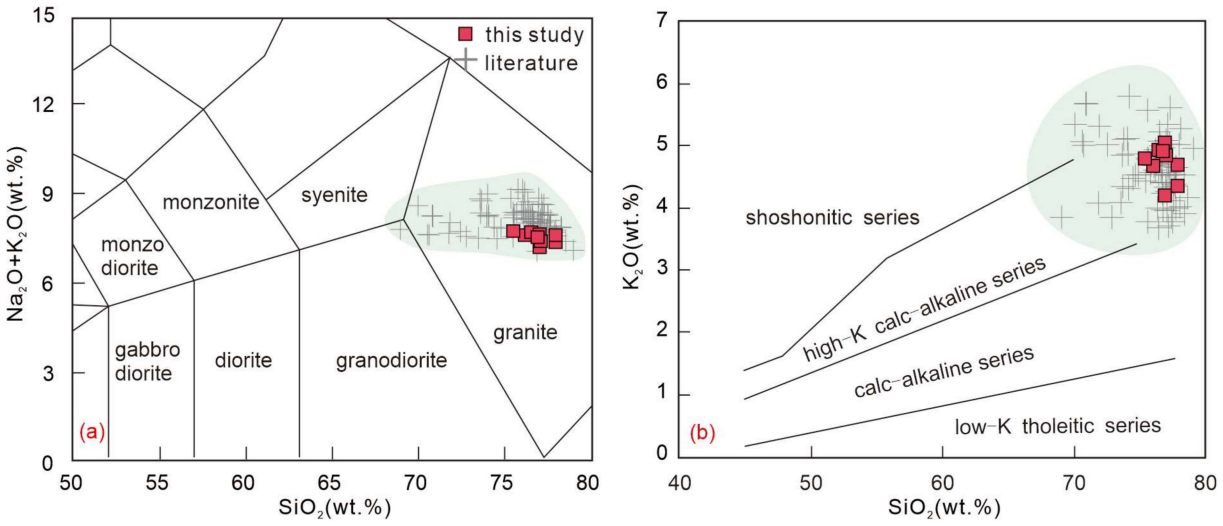

Figure 4. Whole-rock SiO_2 vs. $Na_2O + K_2O$ (**a**) and SiO_2 vs. K_2O (**b**) classification diagrams of the granite phases from Kese granite in BNMB, Central Tibet ((**a**) after [53]; (**b**) after [54]; the literature from [40]).

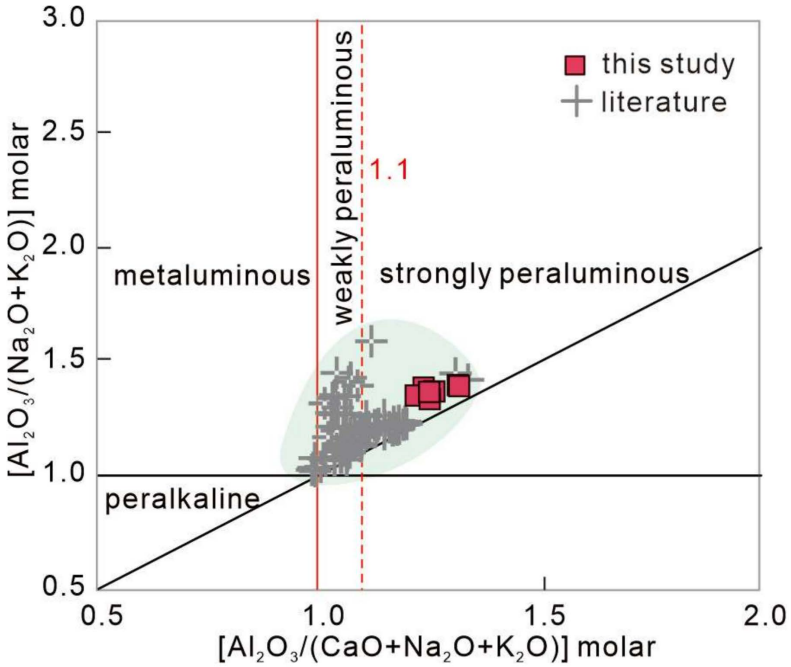

Figure 5. A/CNK vs. A/NK diagram of Kese granite in BNMB, Central Tibet (after [55]).

All the samples were characterized by similar nearly flat REE patterns ($(La/Yb)_N$ = 3.14~5.80), especially in heavy rare earth elements (HREEs) ($(Gd/Lu)_N$ = 1.01~1.39) with strongly negative Eu anomalies (Eu/Eu* = 0.24~0.52)). In the primitive mantle-normalized trace element diagrams, an enrichment in large ion lithophile elements (LILEs; e.g., Rb, Th, U, and K) was observed in the samples, while a depletion was detected in high-field-strength elements (HFSEs), with Ba, Nb, Ta, P, and Ti showing particularly prominent negative anomalies (Figure 6). Moreover, both major and minor element features of Kese granite were similar to the typical highly fractionated granite in China.

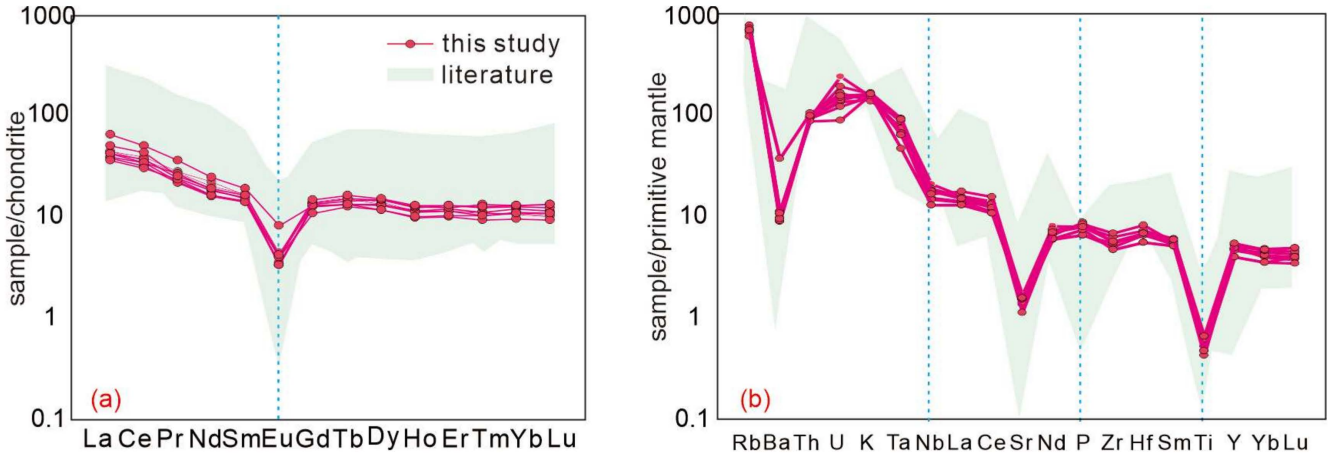

Figure 6. Chondrite-normalized REE patterns (**a**) and primitive-mantle normalized spider diagrams (**b**) for Kese granite in BNMB, central Tibet (the chondrite-normalizing values and primitive mantle-normalizing values are from [56]).

Using the zircon saturation thermometer [57], it can be determined that the Kese granite crystallizes at temperatures ranging from 721 to 745 °C, with an average temperature of 731 °C (Table 2).

4.3. Zircon Hf Isotopes

Table 3 shows the Lu–Hf isotopes of representative zircon grains in situ measured from the sample. For the calculation of $\varepsilon_{Hf}(t)$, t_{DM1}(Hf), and t_{DM2}(Hf) values, we used the zircon U–Pb ages obtained in this study (127.8 Ma). All fifteen analyses of zircons from the Kese granite were characterized by highly enriched zircon Hf isotopic compositions with a broad variation in $\varepsilon_{Hf}(t)$ from −12.8 to +0.3. The zircons also had old two-stage Hf model ages (t_{DM2}) of 1156~1993 Ma (Figure 7).

Table 3. LA–ICP–MS zircon Hf isotopic analyses for the samples of Kese granite in Baingoin area, central Tibet.

Spot	Age (Ma)	$^{176}Yb/^{177}Hf$	2σ	$^{176}Lu/^{177}Hf$	2σ	$^{176}Hf/^{177}Hf$	2σ	$^{176}Lu/^{177}Hf(t)$	$\varepsilon_{Hf}(t)$	t_{DM} (Ma)	t_{DM2} (Ma)	$f_{Lu/Hf}$
D17R23_2	128.2	0.022649	0.000424	0.000692	0.000008	0.282515	0.000013	0.28251	−6.3	1034	1587	−0.98
D17R23_3	120.4	0.068499	0.001573	0.002071	0.000048	0.282712	0.000014	0.28271	0.3	788	1156	−0.94
D17R23_4	127.0	0.054868	0.000534	0.001678	0.000005	0.282687	0.000014	0.28268	−0.4	815	1206	−0.95
D17R23_7	129.2	0.046389	0.000727	0.001415	0.000014	0.282640	0.000012	0.28264	−2.0	876	1310	−0.96
D17R23_8	134.6	0.045945	0.000323	0.001477	0.000006	0.282695	0.000014	0.28269	0.1	799	1182	−0.96
D17R23_9	128.0	0.057724	0.000563	0.001825	0.000008	0.282690	0.000014	0.28269	−0.2	813	1199	−0.95
D17R23_10	127.6	0.042850	0.000138	0.001396	0.000006	0.282692	0.000013	0.28269	−0.1	801	1193	−0.96
D17R23_11	130.5	0.033702	0.000268	0.001161	0.000011	0.282559	0.000012	0.28256	−4.8	985	1490	−0.97
D17R23_12	125.7	0.026348	0.000366	0.000913	0.000014	0.282478	0.000012	0.28248	−7.7	1091	1673	−0.97
D17R23_13	129.3	0.046984	0.000294	0.001545	0.000015	0.282581	0.000015	0.28258	−4.1	964	1444	−0.95
D17R23_14	123.0	0.074529	0.000722	0.002417	0.000029	0.282339	0.000015	0.28233	−12.8	1339	1993	−0.93
D17R23_16	126.4	0.047445	0.000561	0.001547	0.000014	0.282575	0.000018	0.28257	−4.3	972	1458	−0.95
D17R23_17	125.1	0.061175	0.000373	0.001977	0.000008	0.282646	0.000014	0.28264	−1.9	880	1301	−0.94
D17R23_19	131.2	0.050809	0.000363	0.001645	0.000008	0.282637	0.000013	0.28263	−2.0	886	1317	−0.95
D17R23_21	132.6	0.064287	0.000967	0.002039	0.000026	0.282605	0.000015	0.2826	−3.2	942	1392	−0.94

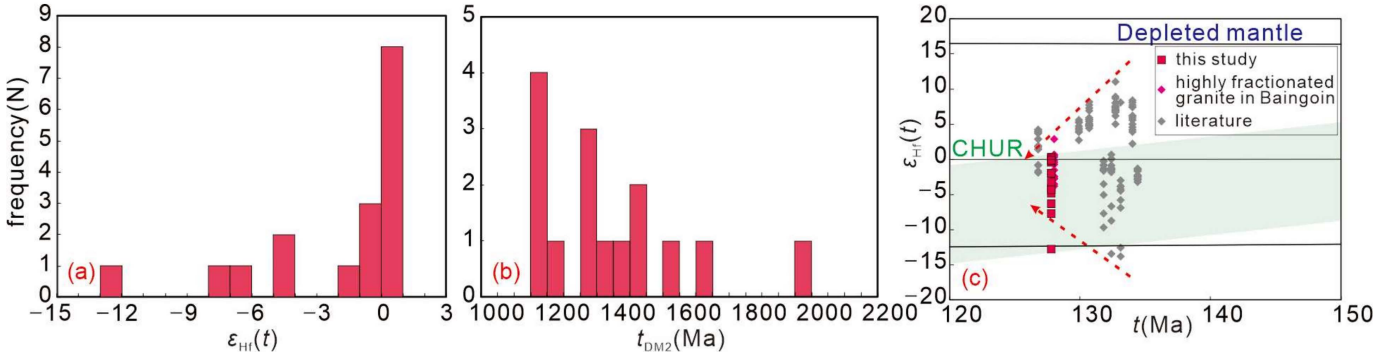

Figure 7. Histograms of $\varepsilon_{Hf}(t)$ (**a**), t_{DM2} (**b**), and Hf isotopic compositions of zircons (**c**) from granitoids of Baingoin area in BNMB, central Tibet ((**c**) data sources: highly fractionated granite in Baingoin from [40], others from [23,37]).

4.4. Whole-Rock Sr–Nd Isotopes

Table 2 summarizes the results of the whole-rock Sr–Nd isotope analyses conducted on four samples. Based on the crystallization age of magma, the initial Sr and Nd isotopic ratios were corrected (127.8 Ma). Two samples of the Kese granite are characterized by high $^{87}Rb/^{86}Sr$ ratios (32.2~34.7), indicating that the initial $^{87}Sr/^{86}Sr$ ratios cannot be used in petrogenetic discussion [58,59]. Additionally, the two samples display slightly heterogeneous Sr isotopic compositions [$(^{87}Sr/^{86}Sr)_i$ ranging from 0.7089 to 0.7253, but relatively homogeneous Nd isotopic compositions, with $\varepsilon_{Nd}(t)$ values of −7.86 and −7.74 (Figure 8) and corresponding two-stage Nd model ages of 1545 Ma and 1552 Ma.

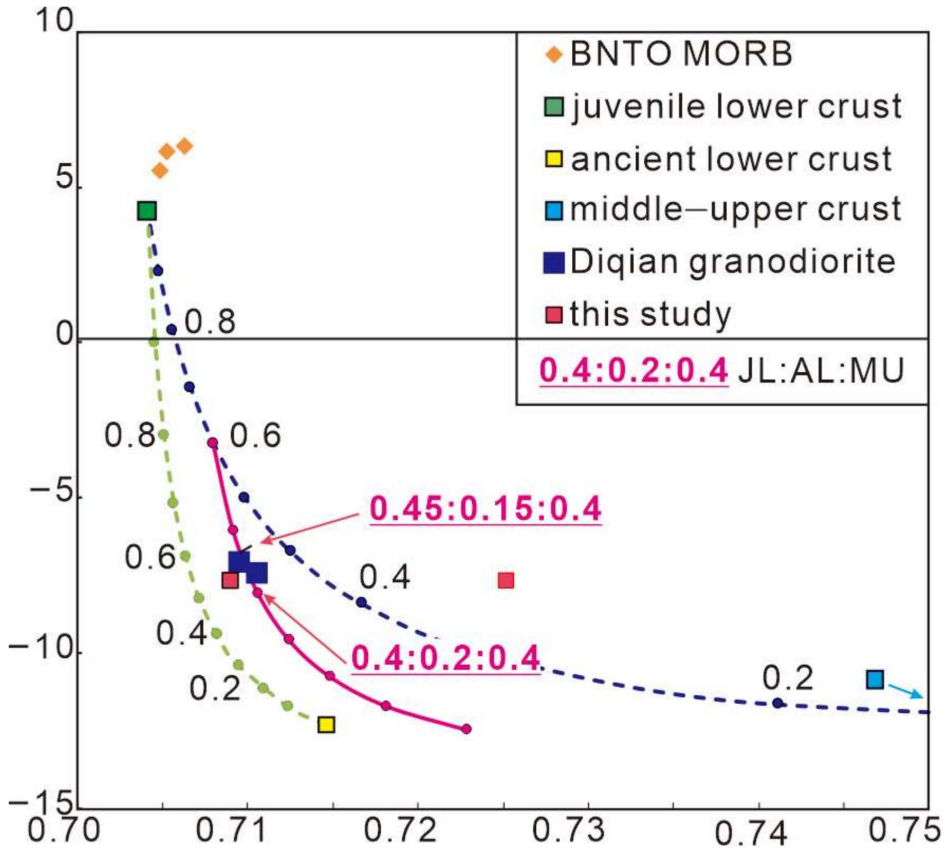

Figure 8. Plot of $(^{87}Sr/^{86}Sr)_i$ vs. whole-rock $\varepsilon_{Nd}(t)$ of the samples from the Kese granite. The compositions of end-members used for mixing calculations include the juvenile lower crust (130 Ma Yanhu basalt, [60]), the ancient lower crust-derived Maiga granodiorite in the central Lhasa terrane [61], and the ancient middle–upper crust-derived Nizhong muscovite monzogranite in the central Lhasa terrane [62]. JL, juvenile lower crust; AL, ancient lower crust; MU, middle–upper crust.

5. Discussion

5.1. Petrogenetic Type of Kese Granite

Historically, amphibole, cordierite, and alkaline melamines were generally considered to be the main distinguishing characteristics and evidence of I-, S-, and A-type granites [63]. Due to the absence of these minerals in Kese granite, the chemical composition is the most objective criterion for identifying granite types. In the discrimination diagrams of the genetic type (Ce, K_2O/MgO, $K_2O + Na_2O$, and Zr vs. $10^4 \times Ga/Al$) (Figure 9), Kese granite falls into the A-type or the area close to A-type granite due to relatively high Ga/Al ratios [62]. However, it is difficult to distinguish A-type granites from the highly fractionated I/S-type granites with $SiO_2 > 72\%$ due to the similarity in both mineral and geochemical compositions [64–67]. The Kese granite contains high concentrations of SiO_2 and total alkalis but low Fe, Mg, and Ca contents and K/Rb ratio; relative enrichment in Rb, Th, U, and Pb; and depletion in Ba, P, and Ti compared with primitive mantle (Figure 6). These features indicate that the granite was formed from highly fractionated granitic magmas [68–72]. Further, a single-stage partial melting will not produce granites with extremely low Sr (less than 100 ppm) and high Rb contents, so Kese granite may undergo intense fractional crystallization [73,74].

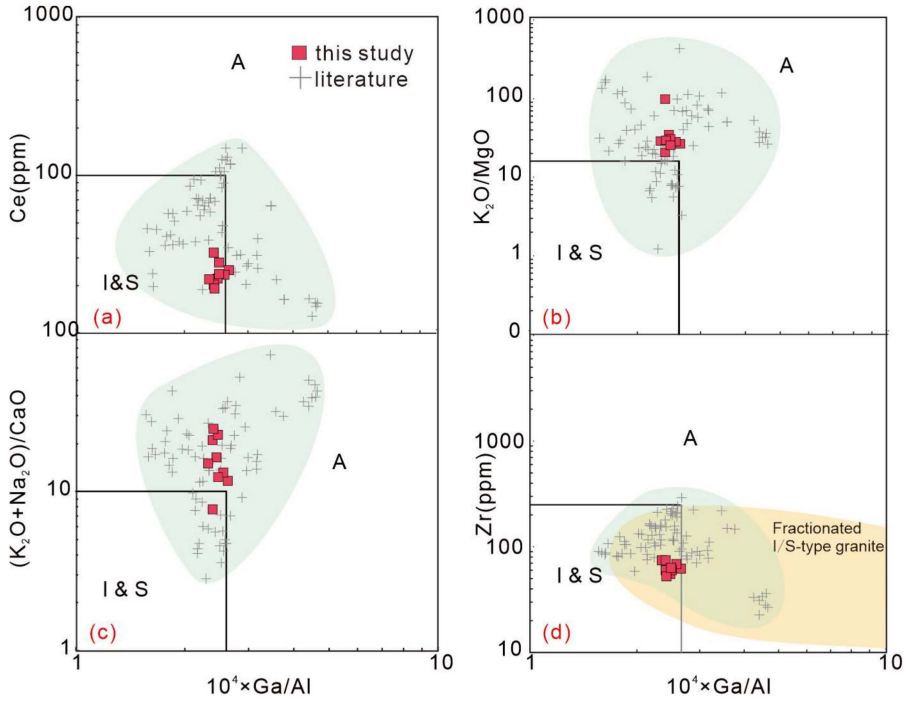

Figure 9. Discrimination diagrams of genetic type for Kese granite in BNMB, central Tibet (after [64]; (**a**–**c**), Kese, granite shows similar features in high Ga/Al values with highly fractionated and A-type granites; (**d**), I/S-type fractionated granite data after [10]).

Kese granite has low concentrations of Ba, Nb, La, Ce Zr, and Y; a relatively low zircon saturation temperature ([57], 721~745 °C); and is depleted in HFSEs, which is inconsistent with features of A-type granite [75,76]. During magmatic differentiation, granitic magma increases the concentration of Li, Rb, and Cs, which is similar to the characteristics of Kese granite [2,77]. Zr/Hf and Nb/Ta ratios usually stay constant during the evolution of common magmatic systems due to their identical geochemical features [10,78]; however, the ratios decrease when magma experiences intense differentiation [79–84]. Some key parameters of Kese granite's differentiation index (DI) deviate from those of chondrites, suggesting highly fractionated characteristics. Furthermore, Kese granite exhibits typical tetrad effects (TE_{1-3} = 1.08~1.13) in the chondrite-normalized REE pattern (Figure 10). A highly fractionated granite whose geochemical behavior has been modified by hydrothermal processes exhibits a special distribution pattern of REEs as a result of melt–fluid interactions, which are common features of highly fractionated granites [85–87]. Therefore, based on the similarity in geochemistry between Kese granite and other highly fractionated granites in China, such as the discrimination diagrams (Figure 11) and high DI (90.4~94.9; calculated by CIPW), we conclude that Kese granite is highly fractionated granite.

Recent studies suggest that the fractional crystallization of amphibole and pyroxene (A/CNK < 1.0) will result in increased A/CNK ratios of residual magma, as many of the strongly peraluminous granites worldwide have largely been derived from igneous sources (I-type granite) [66,88–90]. In addition, it has been proposed that I-type granites gradually change from metaluminous to peraluminous with increasing SiO_2, whereas the A/CNK ratios of S-type granites slightly drop or remain constant [91,92]. Kese granite is consistent with the former trend, indicating an I-type granite feature (Figure 12j). Experimental petrology suggests that the relationship between SiO_2 and P_2O_5 constitutes an important indicator of genetic type, and certain trace elements, such as Th and Y, are found to change greatly in different granitic melts [69,88,93]. Kese granite exhibits all of the relevant geochemical characteristics of an I-type granite (Figure 13). Consequently, it is reasonable to conclude that Kese granite belongs to the highly fractionated I-type granite.

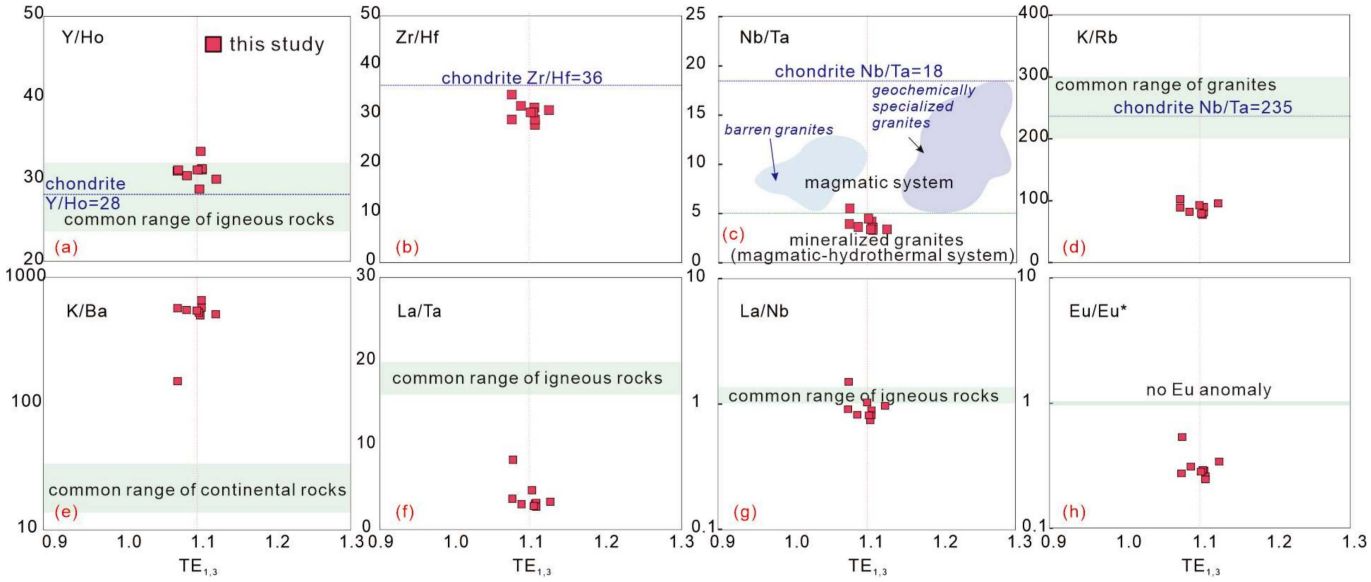

Figure 10. Variations in several key elemental ratios as indicators of differentiation from Kese granite in BNMB, central Tibet ((**a**–**h**), multiple element ratios indicate that the Kese granite has undergone a differentiation process). $TE_{1,3} = (TE_1 \times TE_3)^{0.5}$, $TE_1 = (Ce/Ce^* \times Pr/Pr^*)^{0.5}$, $TE_3 = (Tb/Tb^* \times Dy/Dy^*)^{0.5}$ [94]. Data sources: chondrite data are from [56], range data of magmatic rocks, granitoids, and continental rocks are from [3].

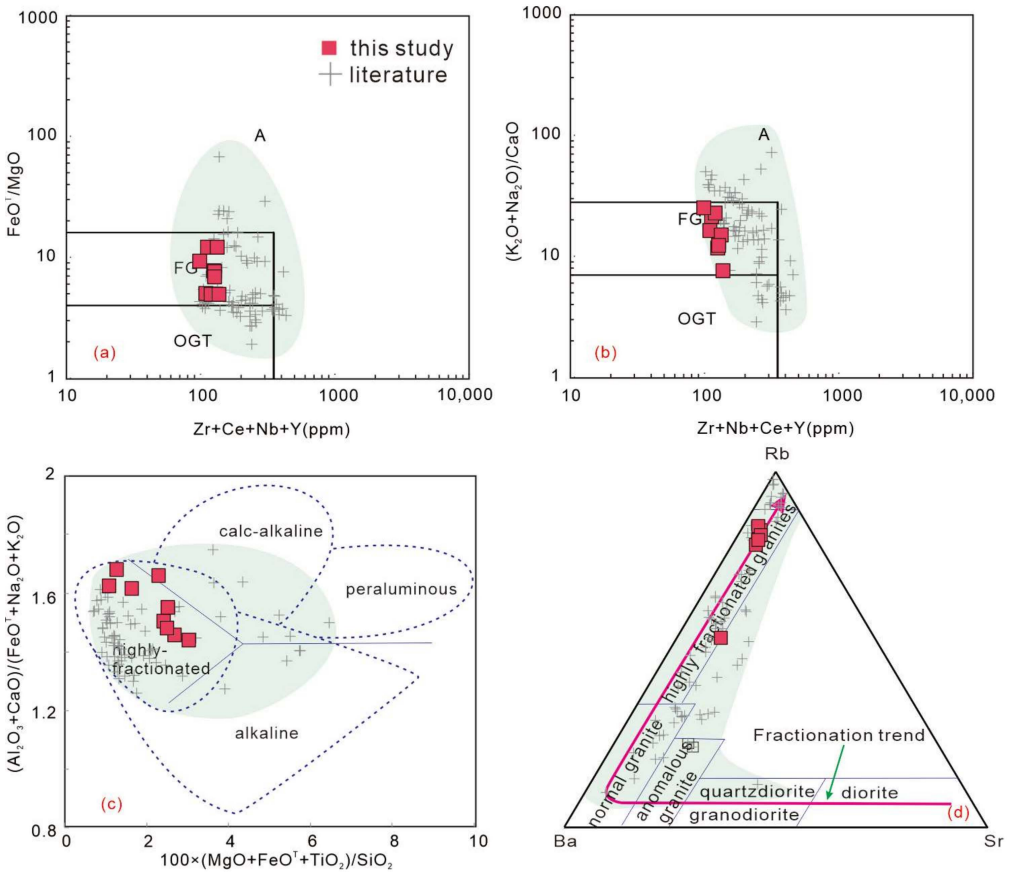

Figure 11. Discrimination diagrams for Kese highly fractionated granite in BNMB, central Tibet ((**a**,**b**), [64]; FG = fractionated I-, S-, and M-type granite; OGT = unfractionated I-, S-, and M-type granite; (**c**), [95]; (**d**), [96]).

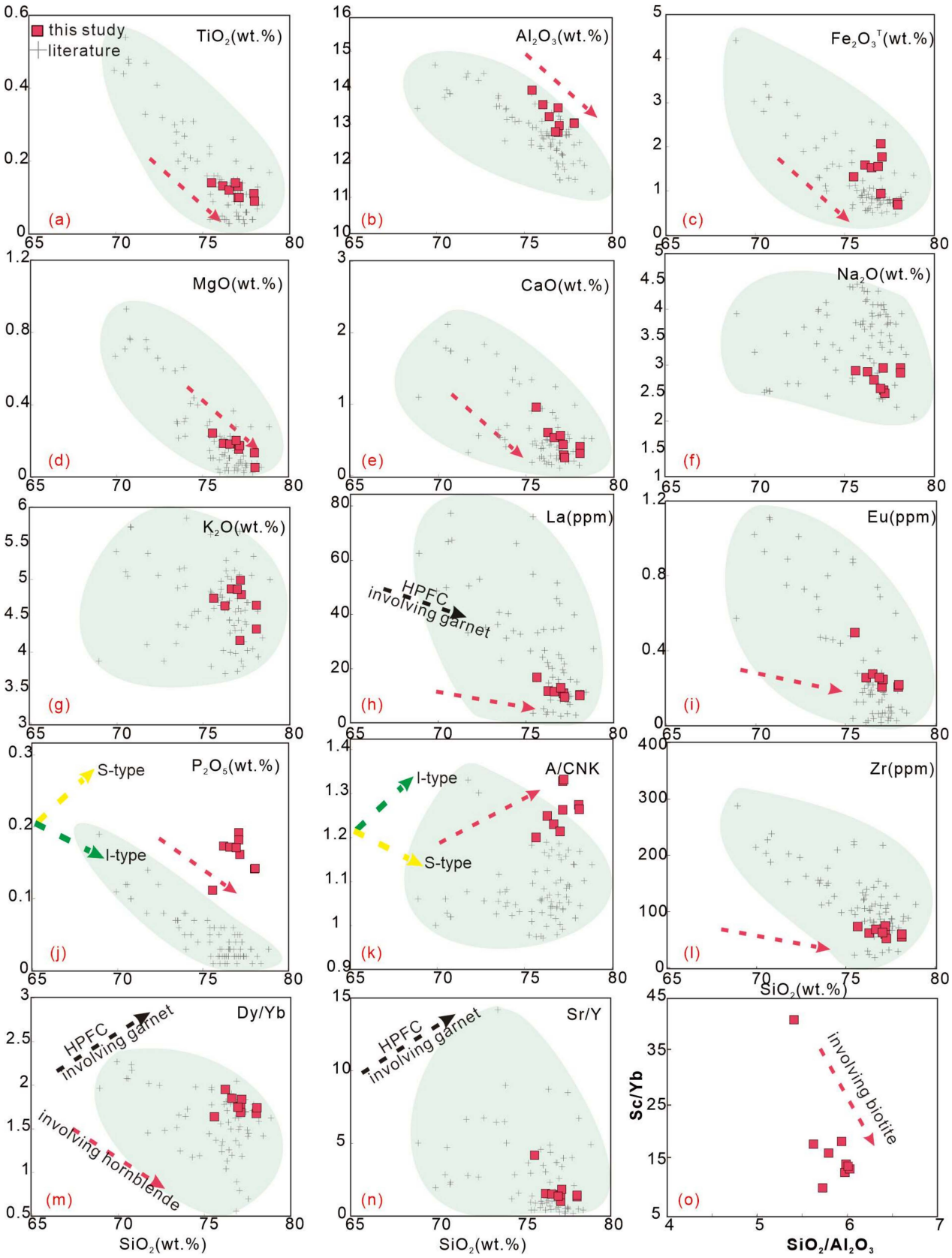

Figure 12. Harker diagrams (**a**–**n**) and Sc/Yb vs. SiO^2/Al^2O^3 diagram (**o**) for Kese granite in BNMB, central Tibet; HPFC, high-pressure fractional crystallization.

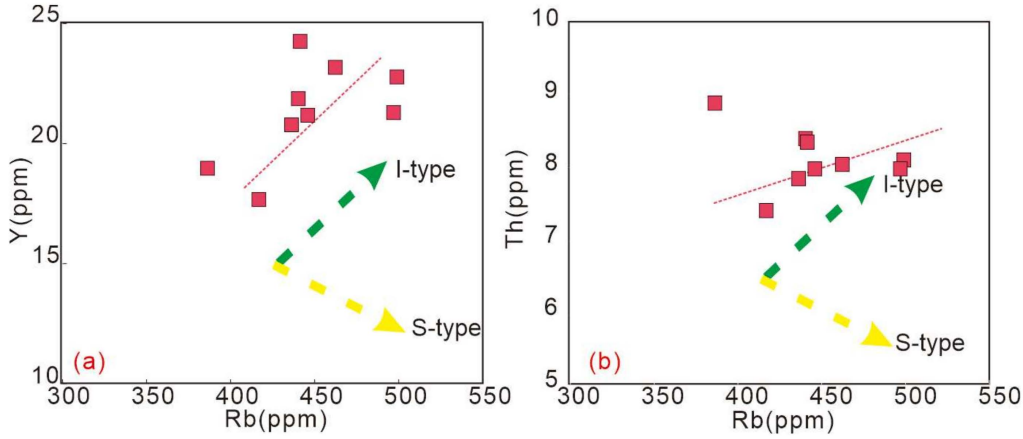

Figure 13. Y vs. Rb and Th vs. Rb diagrams for Kese granite in BNMB, central Tibet (both the positive correlations of Y-Rb (**a**) and Th-Rb (**b**) indicate that Kese granite belongs to I-type granite; after [88]).

5.2. Petrogenesis of Kese Granite

5.2.1. Magma Source Characteristics

With regard to the origin of highly fractionated I-type granite, two primary petrogenetic mechanisms have been proposed: (1) a complete crystallization fractionation process of mantle-derived mafic magma; (2) partial melting of crust materials (with involvement of mantle-derived materials) accompanied by subsequent fractional crystallization [88,90,97–99]. In light of the extensive fractionation, whole-rock geochemical data cannot reflect the characteristics of the granite's original magma due to the limited effect of magmatic differentiation on the Sm/Nd and Lu/Hf ratios in highly fractionated granite; it is possible to distinguish the magma source using Nd and Hf isotopes [32,100]. Hence, petrogenesis research requires integrating field observation, petrography, and isotopic data.

First, the former mechanism should be precluded for Kese granite. Researchers have found that a fractional crystallization process can produce only one part of felsic granitoids from nine parts of mafic magmatic bodies [101,102]. However, it seems unlikely that the Kese granite's main magma is derived from the fractional crystallization of mafic magma due to its high SiO_2 contents (>74 wt%). Furthermore, mafic lavas of large volume do not exist in the region that could have contributed to fractional crystallization.

Based on Kese granite's narrow variation in the Nd isotopic composition (Figure 8, Table 2) and the fact that both $\varepsilon_{Nd}(t)$ and $\varepsilon_{Hf}(t)$ values are largely negative, except two small positive values for Hf isotope (+0.1 and +0.3), it seems unlikely that the granite derives from heterogeneous ancient crust materials. The $\varepsilon_{Hf}(t)$ values of the zircon vary from −12.8 to +0.3 with a variation of up to 13 epsilon units, which represents a complex magma chamber process involving variation in the composition of the source. As the Hf isotope ratios of the zircons did not change during fractional crystallization, the variation in $\varepsilon_{Hf}(t)$ values of Kese granite could be attributed to both less radiogenic (ancient crustal magma) and radiogenic (mantle-derived or juvenile crust-derived magma) end-members [103]. On the contrary, the Nd isotopic composition of both end-members of Kese granite may undergo a complete mixing, resulting in a homogeneous feature of Kese granite.

As mentioned above, the high $^{87}Rb/^{86}Sr$ ratios (32.2~34.7) of Kese granite resulted in the invalid initial $^{87}Sr/^{86}Sr$ ratios for petrogenetic discussion. Diqian granodiorite is emplaced at 134.4 Ma and adjacent to Kese granite (Figure 1). Due to the long emplaced interval (up to 6.4 Ma), it cannot be assumed that Kese granite was generated directly from the Diqian pluton via fractional crystallization [104], while Diqian granodiorite exhibits similarities with Kese granite in terms of whole-rock $\varepsilon_{Nd}(t)$ (−7.5~−7.1) and zircon $\varepsilon_{Hf}(t)$ (−3.2~−1.3) values [37]. Given the spatial relationship between the two plutons and their isotopic characteristics, it is plausible to conclude that Kese granite formed from the partial melting of the Diqian pluton followed by intensive fractional crystallization or shared a

common magma source. In this sense, Diqian granodiorite can substitute for Kese granite based on its whole-rock Sr–Nd isotopic system.

As indicated by recent geochronological data for the magmatic rocks of the northern Lhasa terrane, the early–middle Early Cretaceous magmatism was relatively weak, with only the Baingoin composite batholith and the Yanhu volcanic rocks being recognized [23]. In a study based on Yanhu volcanic rocks, it was speculated that the ~130 Ma basaltic magma derived from the partial melting of a metasomatized mantle wedge formed the juvenile lower crust with positive whole-rock $\varepsilon_{Nd}(t)$ values [60,105]. Considering the scissor-like diachronous orogeny from east to west, this mafic magma event is likely to correspond to the 134.4 Ma magmatic event in Baingoin, which may be represented by the mafic microgranular enclaves (MMEs) present in Diqian granodiorite [37]. In this paper, we consider the known 130 Ma Yanhu basalt as mantle-derived magma and select the typical rocks derived from the ancient lower and middle–upper continental crustal materials [61,62]. As the juvenile lower crust is formed by underplated mantle-derived mafic magma, Kese granite may derive its magma sources from both the juvenile lower crust and ancient continental crust at different levels. The ancient zircons (analysis locations 15, 20, and 22) may represent the addition of Proterozoic continental crust.

Several experiments have shown that partial melting of low-K metabasalts in the lower crust would result in low-K intermediate to felsic melts with variable concentrations of Na_2O and CaO [106], unlike Kese granite, which has a high affinity for K. In contrast, granitic melts with high SiO_2 and high K_2O/Na_2O ratios should be produced by medium- to high-K basaltic melts [89]. Research has demonstrated that the ~130 Ma basalt in the Yanhu area belongs to medium-K basalts [60,105], consistent with Kese granite (Figure 4b).

As a result, we concluded that Kese granite originated from a complete mixing of melts derived from 40 to 45% juvenile basaltic lower crust melts, 15 to 20% ancient lower crust melts, and 40% middle–upper crust melts. Kese granite then experienced an intense fractional crystallization process. The juvenile lower crust was generated earlier than 134 Ma, as evidenced by 130 Ma Yanhu basalt and MMEs in Diqian granodiorite. Additionally, the mixing magma exhibited a medium- to high-K affinity.

5.2.2. Fractional Crystallization

Primary magmas can undergo crustal contamination during ascent or stay in the crust, which affects their geochemical characteristics [107]. Crustal contamination decreases $\varepsilon_{Nd}(t)$ and increases $(^{87}Sr/^{86}Sr)_i$ values [108]. In the SiO_2 vs. $\varepsilon_{Nd}(t)$ diagrams (unshown), in the absence of a negative correlation, it seems crustal contamination has a limited impact on magma evolution. The differentiation of minerals may be reflected by the following explanations: (1) in the Ti-rich minerals, only residual rutile would increase the $(La/Yb)_N$ ratio and decrease the Nb/La ratio (Figure 12a) [109]. As shown by the diagram, the negative correlation between TiO_2 and SiO_2 may reflect the differentiation rather than the residue of rutile (Figure 14a); (2) negative correlation between P_2O_5, Zr, and SiO_2 and the depletion of P and Zr may be due to the differentiation of apatite and zircon (Figure 12j,l) [65]; (3) with increasing SiO_2, MgO, $Fe_2O_3{}^T$, and CaO decreased, indicating that mafic minerals have been fractionated (Figure 12c–e). Generally, amphibole is an important mineral-bearing middle rare earth element (MREEs) [110], and the MREE pattern with approximately equal Ho_N–Yb_N shows that amphibole may have played a role in fractional crystallization (Figure 5a); (4) it has generally been shown that garnet crystallization fractionation produces unique geochemical features, which result in a positive correlation between the Dy/Yb vs. SiO_2 and Sr/Y vs. SiO_2, and a negative correlation between La and SiO_2 contents [111,112], but the former phenomenon was not clearly observed in the Kese granite (Figure 12m,n); (5) the $(La/Yb)_N$ vs. La diagram (Figure 14b) supports the idea that allanite and monazite can be fractionated, and previous studies suggested that monazite may influence the Th and light rare earth elements (LREEs) content in peraluminous granites [113]. Thus, the relationships (LREEs vs. Th and $(La/Yb)_N$ vs. La) show that monazite played a key role in controlling the La contents and caused differentiation (Figure 14b,c) [113,114]. Furthermore,

the heterogeneous REEs displayed in chondrite-normalized REE patterns (Figure 6a) are led by the differentiation of these accessory minerals; (6) meanwhile, garnet is enriched in heavy rare earth elements (HREEs), and the HREE pattern of Kese granite indicates that garnet was unlikely to be a residue mineral [106]. Fractionation of garnet will show an increase in Dy/Yb ratios simultaneously, whereas fractionation of amphibole will show a decrease [115]; as shown in Figure 12m, it appears that amphibole is the differentiation mineral as opposed to garnet; (7) significant negative Eu, Ba, and Sr anomalies and correlations with Al_2O_3 and Eu vs. SiO_2 (Figure 12b,i) are in agreement with the fact that this granite was formed by fractional crystallization of plagioclase (Figure 14d), resulting in high Rb/Sr ratios and Rb concentrations in the residual magma; (8) biotite is an Al-bearing mineral with a low partition coefficient for Yb but a high value for Sc ($D_{Yb}^{biotite/melt}$ = 0.12, $D_{Sc}^{biotite/melt}$ = 42.4) [116]. In Kese granite, there is a negative correlation between Sc/Yb and SiO_2/Al_2O_3 that suggests biotite is a significant fractionation mineral (Figure 12o); (9) a lack of correlation in Na_2O and K_2O vs. SiO_2 diagrams indicates that there is no evidence for fractional crystallization of alkaline feldspars in Kese granite (Figure 12f,g).

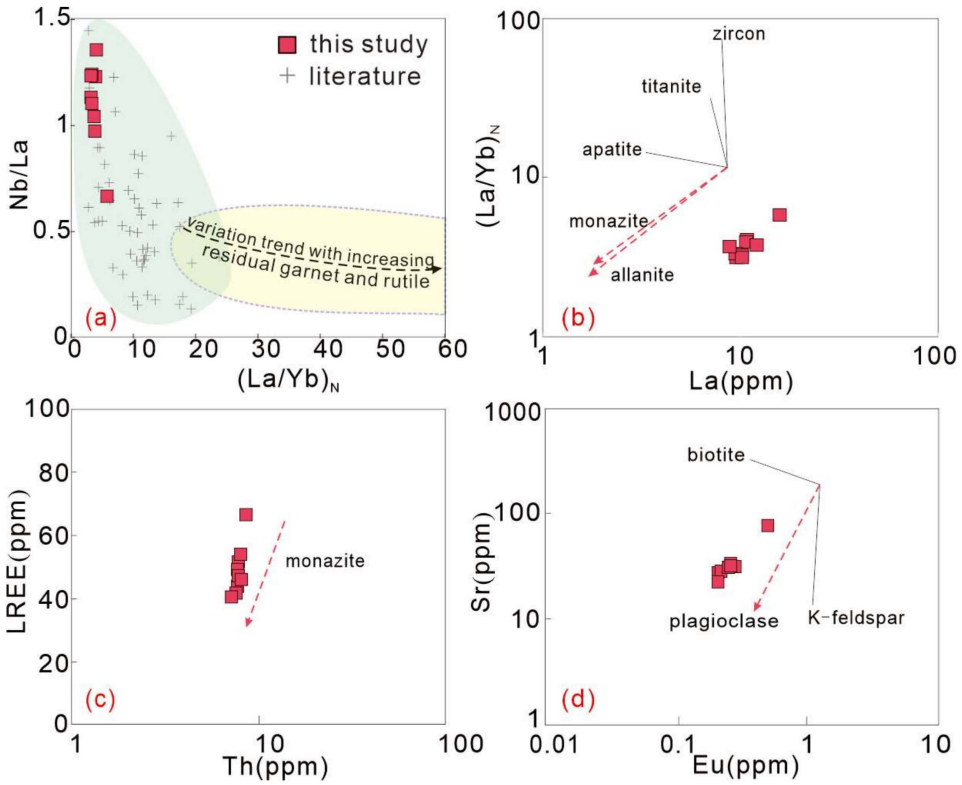

Figure 14. Nb/La vs. $(La/Yb)_N$ (**a**), $(La/Yb)_N$ vs. La (**b**), LREE vs. Th (**c**), and Sr vs. Eu (**d**) diagrams for Kese granite in BNMB, central Tibet ((**a**), after [109], data sources as Figure 4; (**b**,**c**), after [117]; (**d**), after [118]).

In summary, during the evolution of the magma, mafic minerals, plagioclase, and several accessory minerals were fractionated. In contrast, garnet and alkaline feldspars were not involved in the process.

5.3. Tectonic Implication

A timeline from the Middle Jurassic to the Late Cretaceous remains highly controversial for the time of the continental collision between the Qiangtang and Lhasa terranes [23,119,120], depending on the methods, areas, and criteria adopted.

In general, the formation of high-K calc-alkaline, highly fractionated I-type granite can occur at various stages during a whole orogeny cycle: (1) subduction-related

continental arc settings such as the Andean type [2], (2) continental collision setting after the closure of the subducted oceanic lithosphere [31,121], and (3) extension stages of post-orogenic setting [10,122].

In light of these diverse tectonic settings, the continental arc setting is the first that can be excluded for highly fractionated I-type granites. Generally, continental arcs produce large felsic batholiths as a result of fractional crystallization, which results in a wide variety of rock types ranging from gabbro and diorite to granite with varying silica contents, similar to the Gangdese arc in Tibet and western North America [2,18,123]. While no contemporaneous mafic and intermediate plutons have been reported in the northern Lhasa terrane, the volume and the silica content of Kese granite are relatively limited, unlike highly fractionated granite in a continental arc setting related to subduction.

In contrast, collision-related highly fractionated granite is typically sparsely scattered and shows monochromatic chemical characteristics and a small proportion of magma derived from the mantle [124]. As far as these characteristics are concerned, Kese granite displays many of the same characteristics as highly fractionated granite in collision settings.

The Duoni (including Duba) formation is widely distributed in a series of Early Cretaceous sedimentary basins in Garze, Nima, Selin Co, Baingoin, Lunpola, and Dingqing area of northern Lhasa terrane, and research indicates that it was part of a Cretaceous peripheral foreland basin, which eventually migrated southward as a result of the collision between the Qiangtang and Lhasa terranes [119,125–129]. In particular, Lai et al. [128] propose that the Duoni formation in the North Baingoin basin originated from the BNSZ and southern Qiangtang terrane and displayed an upward transition from a shallow shelf and deltaic environment to a coarse-grained siliciclastic fluvial sedimentation controlled by the Lhasa–Qiangtang collision (earlier than 122 Ma). The Qumeile granitic pluton (128 Ma) in the Baingoin area intruded into the Duoni formation in the north and developed hornstone in the contact zone (Figure 1) [40], meaning that the contemporaneous Kese granite is younger than the Duoni formation's initial deposit. The zircon U–Pb ages based on the interbedded volcanic rocks and detritus zircons indicate that the Duoni formation lasted for at least 114 Ma [127,130]. Consequently, Kese granite was deposited during the Duoni formation in the Baingoin area, indicating that it was generated during the collision, which had already occurred by 128 Ma.

Moreover, east of Baingoin, around the Dingqing area, the Lagongtang formation was assumed to deposit in a peripheral foreland basin system resulting from the Lhasa–Qiangtang collision, which began around 140 Ma in the Dingqing region [129]. To the west of Baingoin, in the Nyima basin, the geological and geochronologic evidence suggests contractional deformation and sedimentation have occurred. A number of Jurassic to Lower Cretaceous ($\leq$125 Ma) marine sedimentary rocks have been transposed and elevated above sea level by ca. 118 Ma [125]. Although it remains disputed whether southward subduction under the Lhasa terrane existed [23], it is reasonable to infer that the Lhasa–Qiangtang collision took place in the Baingoin area before 128 Ma based on scissor-like diachronous collision models.

5.4. Continental Crust Evolution

Research on zircon Hf isotopic compositions indicates that mantle materials have contributed to 30%~100% of the formation of northern Lhasa terrane, and the $\varepsilon_{Hf}(t)$ decreases towards the eastern part of the terrane, indicating more ancient crustal materials proportions from the Lhasa microcontinent [18]. Magmatic rocks from the Baingoin area were observed to have both negative and positive zircon $\varepsilon_{Hf}(t)$ values between 140 Ma and 125 Ma (Figure 7c) [23,37,40]. The ~130 Ma basalt in Yanhu and the mantle-derived MMEs hosted by the 134.4 Ma granitic pluton in Baingoin indicate that a high proportion of mantle-derived magma contributed to the sources, as indicated by the positive zircon $\varepsilon_{Hf}(t)$ values [37,60]. Consequently, the northern Lhasa terrane underwent a continental growth process at approximately 134 Ma. Meanwhile, some contemporaneous magmatic rocks appear to have negative $\varepsilon_{Hf}(t)$ values, which have also been attributed to an ancient

crustal anatexis [18]. Based on these results, it can be concluded that both crustal growth and reworking took place between 140 and 130 Ma.

As a result of a high degree of mixing and differentiated process, zircon $\varepsilon_{Hf}(t)$ values of the ~128 Ma granitic plutons in the Baingoin area are much more concentrated. Despite some zircons showing depleted Hf isotopic compositions, as indicated by the analysis above (Section 5.2.1), these highly fractionated granites are the result of the melting of both juvenile and ancient crusts represented by the zircons from Proterozoic materials (Figure 3a). In continental collision settings, the partial melting of intra-crustal mafic sources can lead to differentiation of the lower crust by extracting SiO_2-rich melts as a result of crustal thickening and heating following the accumulation of heat-producing elements [131,132]. In conjunction with the refinement of ancient crustal materials, this resulted in the chemical differentiation of the pre-existing crust, which subsequently shifted its composition toward that of mature continental crust [121]. In this way, we infer that during the collision of the Lhasa–Qiangtang terranes, the reworking of juvenile and ancient continental crust at various levels represents the main mode of crustal evolution in the northern Lhasa terrane, as indicated by the presence of highly fractionated granites at Baingoin.

5.5. Evaluation of the Economic Potentiality of Kese Granite

As mentioned above, numerous deposits share genetic connections with highly fractionated granites, including the giant Dahutang W deposit in south China, the Shamai W deposit in central Asia orogenic belt, the Sn-W deposits in the Khuntan Batholith of northern Thailand [3], Nb–Ta deposits in the Lingshan complex pluton and the 414 pluton of Yashan in south China [7,118], the Mo deposit in the Liyuantang pluton of the Qinling orogenic belt [133], and the super-large Cuonadong Be–W–Sn deposit [14,134].

Given the difficulty of ore prospecting and exploration on the rise, discriminating between barren and fertile intrusions is one of the biggest challenges when searching for granite-related ore deposits. Geochemistry, mineralogy, and texture of granite are considered crucial markers for distinguishing magma differentiation and metallogenic stage, discriminating fertile and barren intrusions, as well as assessing the economic potentiality of the hidden and poorly outcropped plutons [135–137]. Kese granite (except one sample) exhibits low K/Rb ratios (<100), Sr (<35 ppm), and Ba contents (<80 ppm), strongly negative Eu anomalies, and tetrad effects of REEs, which indicate extensive magmatic fluid fractionation processes were involved in the formation of the granite [138]. Furthermore, Rb/Sr ratios would increase when the granite evolves toward more felsic and highly differentiated forms [73], while K/Rb, Na/Ta, and Zr/Hf ratios would exhibit opposite trends [84,139]. The results are consistent with those found in Kese granite (Table 2). Additionally, the ratios of Na/Ta and Zr/Hf are also considered important indicators of the transition from a purely magmatic system to a magmatic–hydrothermal system, with Zr/Hf ratios below 26 and Nb/Ta ratios below 5 considered to be indicators [79,139]. According to the detailed research, most barren granites plot in the area defined by $5 < Nb/Ta < 16$ and $26 < Zr/Hf < 46$ (CHARAC range of [79]), whereas peraluminous granites associated with Sn–W–(U) deposits have comparable Nb/Ta ratios < 5 and Zr/Hf ratios between 18 and 46, while the rare-metal granites have even lower Zr/Hf ratios (<18) [139]. These markers have been applied successfully to the Abu-Diab rare-metal-bearing granites in the Eastern Desert area, Egypt [74]. Na/Ta ratios of Kese highly fractionated granites are less than 5, which is similar to those of Sn–W–(U)-related granites in the magmatic–hydrothermal system rather than that of rare-metals-related granites and barren granites (Figures 10c and 15). As a consequence, our interpretation of the whole-rock geochemistry of Kese granite suggests that the reworking of pre-existing juvenile and ancient crustal materials may provide favorable conditions for a preliminary exploration of Sn–W–(U) deposits in the BNMB.

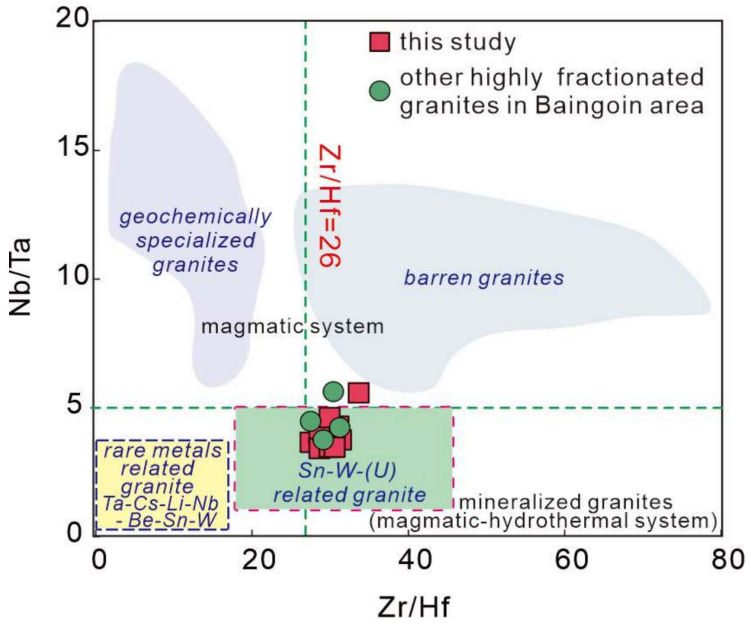

Figure 15. Nb/Ta vs. $TE_{1,3}$ and Nb/Ta vs. Zr-Hf diagrams for Kese granite in BNMB, central Tibet (yellow and green rectangles indicate the areas of rare metals related and Sn-W-(U) related granites, respectively; after [74,139]).

6. Conclusions

1. Kese granite from the BNMB was formed in the middle Early Cretaceous (127.8 ± 1.7 Ma) and is highly fractionated granite;
2. The continental collision of the Lhasa and Qiangtang terranes was initiated prior to 128 Ma and drove the reworking of pre-existing juvenile and ancient materials in different crustal levels;
3. The reworking and increase in maturity of the continental crust in the north Lhasa terrane are considered suitable for preliminary exploration for Sn–W–(U) minerals in the BNMB.

Author Contributions: Conceptualization, N.W. and M.L.; methodology, N.W.; software, N.W. and M.L.; validation, Z.L.; investigation, N.W. and Z.L.; data curation, N.W.; writing—original draft preparation, N.W.; writing—review and editing, M.L. and Z.L.; visualization, N.W.; supervision, Z.L.; project administration, Z.L.; funding acquisition, N.W. All authors have read and agreed to the published version of the manuscript.

Funding: This research was funded by the Special funds of the basic scientific research of the Chinese Academy of Geological Sciences (grants no. JKYQN202331) and China Geological Survey (grants no. DD20230358, DD20230286 and DD20221684).

Data Availability Statement: All data generated during the current study are available in full within this article.

Acknowledgments: We are grateful to two anonymous reviewers and editors of this journal for their valuable suggestions and revisions of the manuscript.

Conflicts of Interest: The authors declare no conflict of interest.

References

1. Tao, J.H.; Li, W.X.; Li, X.H.; Cen, T. Petrogenesis of early Yanshanian highly evolved granites in the Longyuanba area, southern Jiangxi Province: Evidence from zircon U-Pb dating, Hf-O isotope and whole-rock geochemistry. *Sci. China Earth Sci.* **2013**, *56*, 922–939. [CrossRef]
2. Lee, C.T.A.; Morton, D.M. High silica granites: Terminal porosity and crystal settling in shallow magma chambers. *Earth Planet. Sci. Lett.* **2015**, *409*, 23–31. [CrossRef]

3. Jiang, S.H.; Bagas, L.; Hu, P.; Han, N.; Chen, C.L.; Liu, Y.; Kang, H. Zircon U–Pb ages and Sr–Nd–Hf isotopes of the highly fractionated granite with tetrad REE patterns in the Shamai tungsten deposit in eastern Inner Mongolia, China: Implications for the timing of mineralization and ore genesis. *Lithos* **2016**, *261*, 322–339. [CrossRef]
4. Monecke, T.; Dulski, P.; Kempe, U. Origin of convex tetrads in rare earth element patterns of hydrothermally altered siliceous igneous rocks from the Zinnwald Sn–W deposit, Germany. *Geochim. Cosmochim. Acta* **2007**, *71*, 335–353. [CrossRef]
5. Wu, F.Y.; Li, X.H.; Yang, J.H.; Zheng, Y.F. Discussions on the petrogenesis of granites. *Acta Petrol. Sin.* **2007**, *23*, 1217–1238, (In Chinese with English abstract).
6. Wu, F.Y.; Liu, Z.C.; Liu, X.C.; Ji, W.Q. Himalayan Leucogranite: Petrogenesis and implications to orogenesis and plateau uplift. *Acta Petrol. Sin.* **2015**, *31*, 1–36, (In Chinese with English Abstract).
7. Yin, L.; Pollard, P.J.; Shouxi, H.; Taylor, R.G. Geologic and geochemical characteristics of the Yichun Ta-Nb-Li deposit, Jiangxi Province, South China. *Econ. Geol.* **1995**, *90*, 577–585. [CrossRef]
8. Marignac, C.; Cuney, M. Ore deposits of the French Massif Central: Insight into the metallogenesis of the Variscan collision belt. *Miner. Depos.* **1999**, *34*, 472–504. [CrossRef]
9. Zhu, J.C.; Li, R.K.; Li, F.C.; Xiong, X.L.; Zhou, F.Y.; Huang, X.L. Topaz-albite granites and rare-metal mineralization in the Limu District, Guangxi Province, southeast China. *Miner. Depos.* **2001**, *36*, 393–405. [CrossRef]
10. Wu, F.Y.; Liu, X.C.; Ji, W.Q.; Wang, J.M.; Yang, L. Highly fractionated granites: Recognition and research. *Sci. China Earth Sci.* **2017**, *60*, 1201–1219. [CrossRef]
11. Yin, A.; Harrison, T.M. Geologic Evolution of the Himalayan-Tibetan Orogen. *Annu. Rev. Earth Planet. Sci.* **2000**, *28*, 211–280. [CrossRef]
12. Pan, G.T.; Mo, X.X.; Hou, Z.Q.; Zhu, D.C.; Wang, L.Q.; Li, G.M.; Zhao, Z.D.; Geng, Q.R.; Liao, Z.L. Spatial-temporal framework of the Gangdese Orogenic Belt and its evolution. *Acta Petrol. Sin.* **2006**, *22*, 521–533, (In Chinese with English Abstract).
13. Xu, Z.Q.; Dilek, Y.; Cao, H.; Yang, J.S.; Robinson, P.; Ma, C.Q.; Li, H.Q.; Jolivet, M.; Roger, F.; Chen, X.J. Paleo-Tethyan evolution of Tibet as recorded in the East Cimmerides and West Cathaysides. *J. Asian Earth Sci.* **2015**, *105*, 320–337. [CrossRef]
14. Xiang, A.P.; Li, W.C.; Li, G.M.; Dai, Z.W.; Yu, H.J.; Yang, F.C. Mineralogy, isotope geochemistry and ore genesis of the miocene Cuonadong leucogranite-related Be-W-Sn skarn deposit in Southern Tibet. *J. Asian Earth Sci.* **2020**, *196*, 104–358. [CrossRef]
15. Girardeau, J.; Marcoux, J.; Allègre, C.J.; Bassoullet, J.P.; Youking, T.; Xuchang, X.; Yougong, Z.; Xibin, W. Tectonic environment and geodynamic significance of the Neo-Cimmerian Donqiao ophiolite, Bangong-Nujiang suture zone, Tibet. *Nature* **1984**, *307*, 27–31. [CrossRef]
16. Dewey, J.F.; Shackleton, R.M.; Chang, C.F.; Yiyin, S. The tectonic evolution of the Tibetan plateau. *Philos. Trans. R. Soc. Lond. Ser. A Math. Phys. Sci.* **1988**, *327*, 379–413.
17. Zhu, D.C.; Pan, G.T.; Mo, X.X.; Wang, L.Q.; Liao, Z.L.; Zhao, Z.D.; Dong, G.C.; Zhou, C.Y. Late Jurassic-Early Cretaceous geodynamic setting in middle-northern Gangdese: New insights from volcanic rocks. *Acta Petrol. Sin.* **2006**, *22*, 534–546, (In Chinese with English Abstract).
18. Zhu, D.C.; Zhao, Z.D.; Niu, Y.L.; Mo, X.X.; Chung, S.L.; Hou, Z.Q.; Wang, L.Q.; Wu, F.Y. The Lhasa Terrane: Record of a microcontinent and its histories of drift and growth. *Earth Planet. Sci. Lett.* **2011**, *301*, 241–255. [CrossRef]
19. Fan, J.J.; Li, C.; Wu, H.; Zhang, T.Y.; Wang, M.; Chen, J.W.; Xu, J.X. Late Jurassic adakitic granodiorite in the Dong Co area, northern Tibet: Implications for subduction of the Bangong–Nujiang oceanic lithosphere and related accretion of the Southern Qiangtang terrane. *Tectonophysics* **2016**, *691*, 345–361. [CrossRef]
20. Hao, L.L.; Wang, Q.; Wyman, D.A.; Ou, Q.; Dan, W.; Jiang, Z.Q.; Wu, F.Y.; Yang, J.H.; Long, X.P.; Li, J. Underplating of basalticmagmas and crustal growth in a continental arc: Evidence from late Mesozoic intermediate–felsic intrusive rocks in southern Qiangtang, central Tibet. *Lithos* **2016**, *245*, 223–242. [CrossRef]
21. Liu, D.L.; Shi, R.D.; Ding, L.; Huang, Q.S.; Zhang, X.R.; Yue, Y.H.; Zhang, L.Y. Zircon U–Pb age and Hf isotopic compositions of Mesozoic granitoids in southern Qiangtang, Tibet: Implications for the subduction of the Bangong–Nujiang Tethyan Ocean. *Gondwana Res.* **2017**, *41*, 157–172. [CrossRef]
22. Song, Y.; Tang, J.X.; Qu, X.M.; Wang, D.H.; Xin, H.B.; Yang, C.; Lin, B.; Fan, S.F. Progress in the study of mineralization in the Bangongco-Nujiang metallogenic belt and some new recognition. *Adv. Earth Sci.* **2014**, *29*, 795–809, (In Chinese with English Abstract).
23. Zhu, D.C.; Li, S.M.; Cawood, P.A.; Wang, Q.; Zhao, Z.D.; Liu, S.A.; Wang, L.Q. Assembly of the Lhasa and Qiangtang terranes in central Tibet by divergent double subduction. *Lithos* **2016**, *245*, 7–17. [CrossRef]
24. Wang, W.; Zhai, Q.G.; Hu, P.Y.; Chung, S.L.; Tang, Y.; Wang, H.T.; Zhu, Z.C.; Wu, H.; Huang, Z.Q. Simultaneous growth and reworking of the Lhasa basement: A case study from Early Cretaceous magmatism in the north-central Tibet. *Lithos* **2021**, *380–381*, 105863. [CrossRef]
25. Li, G.M.; Qin, K.Z.; Li, J.X.; Evans, N.J.; Zhao, J.X.; Cao, M.J.; Zhang, X.N. Cretaceous magmatism and metallogeny in the Bangong–Nujiang metallogenic belt, central Tibet: Evidence from petrogeochemistry, zircon U–Pb ages, and Hf–O isotopic compositions. *Gondwana Res.* **2017**, *41*, 110–127. [CrossRef]
26. Lin, B.; Zhang, X.G.; Tang, P.; Wang, L.Q.; Santosh, M.; Xi, Z.; Zhang, X.X.; Qi, J.; He, L. Geology and geochronology of the Jinmuguo Mo polymetallic deposit: Implications for the metallogeny of the Bangongco- Nujiang belt of Tibet. *Ore Geol. Rev.* **2021**, *139*, 104460. [CrossRef]
27. Lin, B.; Zou, B.; Tang, P.; He, W.; Liu, Z.Y.; Qi, J.; Li, F.Q.; Chen, L.; Zhang, X.X.; Sun, M. Multiple isotopic dating constrains the time framework (Age) of a porphyry system: A case study from the Sangri Cu-Mo deposit, Bangongco-Nujiang metallogenic belt, Tibet, China. *Ore Geol. Rev.* **2022**, *144*, 104870. [CrossRef]

28. Tang, J.X. Mineral resources base investigation and research status of the Tibet Plateau and its adjacent major metallogenic belts. *Acta Petrol. Sin.* **2019**, *35*, 617–624, (In Chinese with English Abstract). [CrossRef]
29. Wang, Y.; Tang, J.X.; Wang, L.Q.; Li, S.; Danzhen, W.X.; Li, Z.; Zheng, S.L.; Gao, T. Magmatism and metallogenic mechanism of the Ga'erqiong and Galale Cu-Au deposits in the west central Lhasa subterrane, Tibet: Constraints fromgeochronology, geochemistry, and Sr-Nd-Pb-Hf isotopes. *Ore Geol. Rev.* **2019**, *15*, 616–635. [CrossRef]
30. Sun, M.; Tang, J.X.; Chen, W.; Ma, X.D.; Song, Y.; Zhang, Z.B.; Liu, Q.P. Timing and origin of the Shesuo skarn Cu-polymetallic deposit in the northern Lhasa subterrane, central Tibet: Implications for Early Cretaceous Cu (Mo) metallogenesis in the Bangong-Nujiang metallogenic belt. *Ore Geol. Rev.* **2021**, *129*, 103919. [CrossRef]
31. Yang, Z.Y.; Wang, Q.; Zhang, C.; Yang, J.H.; Ma, L.; Wang, J.; Sun, P.; Qi, Y. Cretaceous (~100 Ma) high-silica granites in the Gajin area, Central Tibet: Petrogenesis and implications for collision between the Lhasa and Qiangtang Terranes. *Lithos* **2019**, *324–325*, 402–417. [CrossRef]
32. He, H.Y.; Li, Y.L.; Wang, C.S.; Han, Z.P.; Ma, P.F.; Xiao, S.Q. Petrogenesis and tectonic implications of Late Cretaceous highly fractionated I-type granites from the Qiangtang block, central Tibet. *J. Asian Earth Sci.* **2019**, *176*, 337–352. [CrossRef]
33. Hu, W.L.; Wang, Q.; Yang, J.H.; Tang, G.J.; Ma, L.; Yang, Z.Y.; Qi, Y.; Sun, P. Petrogenesis of Late Early Cretaceous high-silica granites from theBangong–Nujiang suture zone, Central Tibet. *Lithos* **2020**, *402–403*, 105788. [CrossRef]
34. Zhu, D.C.; Zhao, Z.D.; Niu, Y.L.; Dilek, Y.; Hou, Z.Q.; Mo, X.X. The origin and pre-Cenozoic evolution of the Tibetan Plateau. *Gondwana Res.* **2013**, *23*, 1429–1454. [CrossRef]
35. Gao, S.B.; Zheng, Y.Y.; Wang, J.S.; Zhang, Z.; Yang, C. The geochronology and geochemistry of intrusive rocks in Bange area: Constraints on the evolution time of the Bangong Lake-Nujiang ocean basin. *Acta Petrol. Sin.* **2011**, *27*, 1973–1982, (In Chinese with English Abstract).
36. Zhu, D.C.; Mo, X.X.; Niu, Y.L.; Zhao, Z.D.; Wang, L.Q.; Liu, Y.S.; Wu, F.Y. Geochemical investigation of Early Cretaceous igneous rocks along an east–west traverse throughout the central Lhasa Terrane, Tibet. *Chem. Geol.* **2009**, *268*, 298–312. [CrossRef]
37. Li, F.Q.; Tang, J.X.; Wang, N.; Liu, Z.B.; Song, Y.; Zhang, J.; Ma, X.D.; Fu, B.; Li, H.F.; Han, S.H. Petrogenesis and geodynamic implications of early Cretaceous (~130 Ma) magmatism in the Baingoin Batholith, central Tibet: Products of subducting slab rollback. *Acta Geol. Sin.* **2022**, *96*, 1960–1978. [CrossRef]
38. Haider, V.L.; Dunkl, I.; von Eynatten, H.; Ding, L.; Frei, D.; Zhang, L. Cretaceous to Cenozoic evolution of the northern Lhasa Terrane and the Early Paleogene development of peneplains at Nam Co, Tibetan Plateau. *J. Asian Earth Sci.* **2013**, *70–71*, 79–98. [CrossRef]
39. Volkmer, J.E.; Kapp, P.; Horton, B.K.; Gehrels, G.E.; Minervini, J.M.; Ding, L. Northern Lhasa thrust belt of central Tibet: Evidence of Cretaceous-early Cenozoic shortening within a passive roof thrust system? *Geol. Soc. Am. Spec. Pap.* **2014**, *507*, 59–70. [CrossRef]
40. Wang, N.; Liu, Z.B.; Song, Y.; Zheng, W.H.; Li, F.Q.; Teng, L. Geochronology and petrogenesis of highly fractionated Early Cretaceous granite in Baingoin area, Tibet. *Acta Petrol. Sin.* **2020**, *36*, 409–425, (In Chinese with English Abstract). [CrossRef]
41. Hou, K.J.; Li, Y.H.; Tian, Y.R. In situ U-Pb zircon dating using laser ablation-multi ion counting-ICP-MS. *Miner. Depos.* **2009**, *28*, 481–492, (In Chinese with English Abstract).
42. Jackson, S.E.; Pearson, N.J.; Griffin, W.L.; and Belousova, E.A. The application of laser ablation-inductively coupled plasma-mass spectrometry to in situ U–Pb zircon geochronology. *Chem. Geol.* **2004**, *211*, 47–69. [CrossRef]
43. Sláma, J.; Kosler, J.; Condon, D.J.; Crowley, J.L.; Gerdes, A.; Hanchar, J.M.; Horstwood, M.S.A.; Morris, G.A.; Nasdala, L.; Norberg, N.; et al. Plešovice zircon–A new natural reference material for U-Pb and Hf isotopic microanalysis. *Chem. Geol.* **2008**, *249*, 1–35. [CrossRef]
44. Liu, Y.S.; Gao, S.; Hu, Z.C.; Gao, C.G.; Zong, K.Q.; Wang, D.B. Continental and oceanic crust recycling-induced melt-peridotite interactions in the Trans-North China Orogen: U-Pb dating, Hf isotopes and trace elements in zircons from mantle xenoliths. *J. Petrol.* **2010**, *51*, 537–571. [CrossRef]
45. Ludwig, K.R. *ISOPLOT 3.00: A Geochronological Toolkit for Microsoft Excel*; Berkeley Geochronology Center: Berkeley, CA, USA, 2003.
46. Hou, K.J.; Li, Y.H.; Zou, T.R.; Qu, X.M.; Shi, Y.R.; Xie, G.Q. Laser ablation-MC-ICP-MS technique for Hf isotope microanalysis of zircon and its geological applications. *Acta Petrol. Sin.* **2007**, *23*, 2595–2604, (In Chinese with English Abstract).
47. Chu, N.C.; Taylor, R.N.; Chavagnac, V.; Nesbitt, R.W.; Boella, R.M.; Milton, J.A.; German, C.R.; Bayon, G.; Burton, K. Hf isotope ratio analysis using multi-collector inductively coupled plasma mass spectrometry: An evaluation of isobaric interference corrections. *J. Anal. At. Spectrom.* **2002**, *17*, 1567–1574. [CrossRef]
48. Scherer, E.; Münker, C.; Mezger, K. Calibration of the Lutetium-Hafnium Clock. *Science* **2001**, *293*, 683–687. [CrossRef]
49. Griffin, W.L.; Wang, X.; Jackson, S.E.; Pearson, N.J.; O'Reilly, S.Y.; Xu, X.; Zhou, X. Zircon chemistry and magma mixing, SE China: In-situ analysis of Hf isotopes, Tonglu and Pingtan igneous complexes. *Lithos* **2002**, *61*, 237–269. [CrossRef]
50. Yang, Y.H.; Zhang, H.F.; Chu, Z.Y.; Xie, L.W.; Wu, F.Y. Combined chemical separation of Lu, Hf, Rb, Sr, Sm and Nd from a single rock digest and precise and accurate isotope determinations of Lu–Hf, Rb–Sr and Sm–Nd isotope systems using Multi-Collector ICP-MS and TIMS. *Int. J. Mass Spectrom.* **2010**, *290*, 120–126. [CrossRef]
51. Crofu, F.; Hanchar, J.M.; Hoskin, P.W.O.; Kinny, P. Atlas of zircon textures. *Rev. Mineral. Geochem.* **2003**, *53*, 469–500. [CrossRef]
52. Wu, Y.B.; Zheng, Y.F. Genesis of zircon and its constraints on interpretation of U-Pb age. *Chin. Sci. Bull.* **2004**, *49*, 1554–1569. [CrossRef]
53. Middlemost, E.A.K. Naming materials in the magma/igneous rock system. *Earth-Sci. Rev.* **1994**, *37*, 215–224. [CrossRef]
54. Martin, H.; Smithies, R.; Rapp, R.; Moyen, J.-F.; Champion, D. An overview of adakite, tonalite–trondhjemite–granodiorite (TTG), and sanukitoid: Relationships and some implications for crustal evolution. *Lithos* **2005**, *79*, 1–24. [CrossRef]
55. Maniar, P.D.; Piccoli, P.M. Tectonic discrimination of granitoids. *Geol. Soc. Am. Bull.* **1989**, *101*, 635–643. [CrossRef]

56. Sun, S.S.; McDonough, W.F. Chemical and isotopic systematics of oceanic basalts: Implications for mantle composition and processes. In *Magmatism in the Ocean Basins*; Saunders, A.D., Norry, M.J., Eds.; Geological Society: London, UK, 1989; Volume 42, pp. 313–345.
57. Miller, C.F.; McDowell, S.M.; Mapes, R.W. Hot and cold granites? Implications of zircon saturation temperatures and preservation of inheritance. *Geology* **2003**, *31*, 529–532. [CrossRef]
58. Jahn, B.M.; Wu, F.Y.; Chen, B. Massive granitoid generation in Central Asia: Nd isotope evidence and implication for continental growth in the Phanerozoic. *Episodes* **2000**, *23*, 82–92. [CrossRef] [PubMed]
59. Wu, F.Y.; Sun, D.Y.; Li, H.; Jahn, B.M.; Wilde, S. A-type granites in northeastern China: Age and geochemical constraints on their petrogenesis. *Chem. Geol.* **2002**, *187*, 143–173. [CrossRef]
60. Sui, Q.L. Chronology, Petrogenesis, and Tectonic Implication of Magmatic Rocks from Yanhu in Northern Lhasa Terrane, Tibet. Master's Thesis, China University of Geosciences, Beijing, China, 2014. (In Chinese with English Abstract).
61. Zhang, X.Q.; Zhu, D.C.; Zhao, Z.D.; Sui, Q.L.; Wang, Q.; Yuan, S.H.; Hu, Z.C.; Mo, X.X. Geochemistry, zircon U-Pb geochronology and in-situ Hf isotope of the Maiga batholith in Coqen, Tibet: Constraints on the petrogenesis of the Early Cretaceous graniotoids in the central Lhasa Terrane. *Acta Petrol. Sin.* **2012**, *28*, 1615–1634, (In Chinese with English Abstract).
62. Liu, Q.S.; Jiang, W.; Jian, P.; Ye, P.S.; Wu, Z.H.; Hu, D.G. Zircon SHRIMP U-Pb age and petrochemical and geochemical features of Mesozoic muscovite monzonitic granite at Ningzhong, Tibet. *Acta Petrol. Sin.* **2006**, *22*, 643–652, (In Chinese with English Abstract).
63. Chappell, B.W.; White, A.J.R. Two contrasting granite types. *Pacif. Geol.* **1974**, *8*, 173–174.
64. Whalen, J.B.; Currie, K.L.; Chappell, B.W. A-type granites: Geochemical characteristics, discrimination and petrogenesis. *Contrib. Mineral. Petrol.* **1987**, *95*, 407–419. [CrossRef]
65. King, P.; White, A.; Chappell, B.; Allen, C. Characterization and origin of aluminous A-type granites from the Lachlan Fold Belt, southeastern Australia. *J. Petrol.* **1997**, *38*, 371–391. [CrossRef]
66. Wu, F.Y.; Jahn, B.M.; Wilde, S.A.; Lo, C.H.; Yui, T.F.; Lin, Q.; Ge, W.C.; Sun, D.Y. Highly fractionated I-type granites in NE China (I): Geochronology and petrogenesis. *Lithos* **2003**, *66*, 241–273. [CrossRef]
67. Wu, F.Y.; Jahn, B.M.; Wilde, S.A.; Lo, C.H.; Yui, T.F.; Lin, Q.; Ge, W.C.; Sun, D.Y. Highly fractionated I-type granites in NE China (II): Isotopic geochemistry and implications for crustal growth in the Phanerozoic. *Lithos* **2003**, *67*, 191–204. [CrossRef]
68. Sawka, W.N.; Heizler, M.T.; Kistler, R.W.; Chappell, B.W. Geochemistry of highly fractionated I- and S-type granites from the tin-tungsten province of western Tasmania. *Geol. Soc. Am. Spec. Pap.* **1990**, *246*, 161–180. [CrossRef]
69. Chappell, B.W.; White, A.J.R. I- and S-type granites in the Lachlan Fold Belt. *Trans. R. Soc. Edinb. Earth Sci.* **1992**, *83*, 1–26. [CrossRef]
70. Foley, S.F.; Barth, M.G.; A Jenner, G. Rutile/melt partition coefficients for trace elements and an assessment of the influence of rutile on the trace element characteristics of subduction zone magmas. *Geochim. Cosmochim. Acta* **2000**, *64*, 933–938. [CrossRef]
71. Clemens, J.D. S-type granitic magmas—Petrogenetic issues, models and evidence. *Earth Sci. Rev.* **2003**, *61*, 1–18. [CrossRef]
72. Xiong, X.L.; Adam, J.; Green, T.H. Rutile stability and rutile/melt HFSE partitioning during partial melting of hydrous basalt: Implications for TTG genesis. *Chem. Geol.* **2005**, *218*, 339–359. [CrossRef]
73. Halliday, A.N.; Davidson, J.P.; Hildreth, W.; Holden, P. Modelling the petrogenesis of high Rb/Sr silicic magmas. *Chem. Geol.* **1991**, *92*, 107–114. [CrossRef]
74. Sami, M.; Ntaflos, T.; Farahat, E.S.; Mohamed, H.A.; Hauzenberger, C.; Ahmed, A.F. Petrogenesis and geodynamic implications of Ediacaran highly fractionated A-type granitoids in the north Arabian-Nubian Shield (Egypt): Constraints from whole-rock geochemistry and Sr-Nd isotopes. *Lithos* **2018**, *304–307*, 329–346. [CrossRef]
75. Bonin, B. A-type granites and related rocks: Evolution of a concept, problems and prospects. *Lithos* **2007**, *97*, 1–29. [CrossRef]
76. Dall'Agnol, R.; Oliveira, D.C. Oxidized, magnetite-series, rapakivi-type granites of Carajás, Brazil: Implications for classification and petrogenesis of A-type granites. *Lithos* **2007**, *93*, 215–233. [CrossRef]
77. Gelman, S.E.; Deering, C.D.; Bachmann, O.; Huber, C.; Gutiérrez, F.J. Identifying the crystal graveyards remaining after large silicic eruptions. *Earth Planet. Sci. Lett.* **2014**, *403*, 299–306. [CrossRef]
78. Green, T.H. Significance of Nb/Ta as an indicator of geochemical processes in the crust-mantle system. *Chem. Geol.* **1995**, *120*, 347–359. [CrossRef]
79. Bau, M. Controls on the fractionation of isovalent trace elements in magmatic and aqueous systems: Evidence from Y/Ho, Zr/Hf, and lanthanide tetrad effect. *Contrib. Mineral. Pet.* **1996**, *123*, 323–333. [CrossRef]
80. Dostal, J.; Chatterjee, A.K. Contrasting behaviour of Nb/Ta andZr/Hf ratios in a peraluminous granitic pluton (Nova Scotia, Canada). *Chem. Geol.* **2000**, *163*, 207–218. [CrossRef]
81. Linnen, R.L.; Keppler, H. Melt composition control of Zr/Hf fractionation in magmatic processes. *Geochim. Cosmochim. Acta* **2002**, *66*, 3293–3301. [CrossRef]
82. Claiborne, L.L.; Miller, C.F.; Walker, B.A.; Wooden, J.L.; Mazdab, F.K.; Bea, F. Tracking magmatic processes through Zr/Hf ratios in rocks and Hf and Ti zoning in zircons: An example from the Spirit Mountain batholith, Nevada. *Mineral. Mag.* **2006**, *70*, 517–543. [CrossRef]
83. Deering, C.D.; Keller, B.; Schoene, B.; Bachmann, O.; Beane, R.; Ovtcharova, M. Zircon record of the plutonic-volcanic connection and protracted rhyolite melt evolution. *Geology* **2016**, *44*, 267–270. [CrossRef]

84. Dostal, J.; Kontak, D.J.; Gerel, O.; Shellnutt, J.G.; Fayek, M. Cretaceous ongonites (topaz-bearing albite-rich microleucogranites) from Ongon Khairkhan, Central Mongolia: Products of extreme magmatic fractionation and pervasive metasomatic fluid: Rock interaction. *Lithos* **2015**, *236–237*, 173–189. [CrossRef]
85. Zhao, Z.H.; Masuda, A.; Shabani, M.B. Tetrad effects of rare-earth elements in rare-metal granites. *Geochimica* **1992**, *3*, 221–233, (In Chinese with English Abstract).
86. Jahn, B.M.; Wu, F.Y.; Capdevila, R.; Martineau, F.; Wang, Y.X.; Zhao, Z.H. Highly evolved juvenile granites with tetrad REE patterns: The Woduhe and Baerzhe granites from the Great Xing'an (Khingan) Mountains in NE China. *Lithos* **2001**, *59*, 171–198. [CrossRef]
87. Monecke, T.; Kempe, U.; Trinkler, M.; Thomas, R.; Dulski, P.; Wagner, T. Unusual rare earth element fractionation in a tin-bearing magmatic-hydrothermal system. *Geology* **2011**, *39*, 295–298. [CrossRef]
88. Chappell, B. Aluminium saturation in I- and S-type granites and the characterization of fractionated haplogranites. *Lithos* **1999**, *46*, 535–551. [CrossRef]
89. Sisson, T.W.; Ratajeski, K.; Hankins, W.B.; Glazner, A.F. Voluminous granitic magmas from common basaltic sources. *Contrib. Mineral. Pet.* **2005**, *148*, 635–661. [CrossRef]
90. Chappell, B.W.; Bryant, C.J.; Wyborn, D. Peraluminous I-type granites. *Lithos* **2012**, *153*, 142–153. [CrossRef]
91. Clemens, J.D.; Stevens, G. What controls chemical variation in granitic magmas? *Lithos* **2012**, *134–135*, 317–329. [CrossRef]
92. Gao, P.; Zheng, Y.F.; Zhao, Z.-F. Distinction between S-type and peraluminous I-type granites: Zircon versus whole-rock geochemistry. *Lithos* **2016**, *258–259*, 77–91. [CrossRef]
93. Wolf, M.B.; Wyllie, P.J. Dehydration-melting of amphibolite at 10 kbar: The effects of temperature and time. *Contrib. Mineral. Pet.* **1994**, *115*, 369–383. [CrossRef]
94. Irber, W. The lanthanide tetrad effect and its correlation with K/Rb, Eu/Eu∗, Sr/Eu, Y/Ho, and Zr/Hf of evolving peraluminous granite suites. *Geochim. Cosmochim. Acta* **1999**, *63*, 489–508. [CrossRef]
95. Sylvester, P.J. Post-collisional strongly peraluminous granites. *Lithos* **1998**, *45*, 29–44. [CrossRef]
96. Wang, Y.J.; Xing, X.W.; Cawood, P.A.; Lai, S.C.; Xia, X.P.; Fan, W.M.; Liu, H.C.; Zhang, F.F. Petrogenesis of early Paleozoic peraluminous granite in the Sibumasu Block of SW Yunnan and diachronous accretionary orogenesis along the northern margin of Gondwana. *Lithos* **2013**, *182*, 67–85. [CrossRef]
97. DePaolo, D.J. Trace element and isotopic effects of combined wallrock assimilation and fractional crystallization. *Earth Planet. Sci. Lett.* **1981**, *53*, 189–202. [CrossRef]
98. Wyborn, D.; Chappell, B.W.; James, M. Examples of convective fractionation in high-temperature granites from the Lachlan Fold Belt. *Aust. J. Earth Sci.* **2001**, *48*, 531–541. [CrossRef]
99. Li, X.H.; Li, Z.X.; Li, W.X.; Liu, Y.; Yuan, C.; Wei, G.J.; Qi, C.S. U-Pb zircon, geochemical and Sr-Nd-Hf isotopic constraints on age and origin of Jurassic I- and A-type granites from central Guangdong, SE China: A major igneous event in response to foundering of a subducted flat-slab? *Lithos* **2007**, *96*, 186–205. [CrossRef]
100. DePaolo, D.J. Age dependence of the composition of continental crust: Evidence from Nd isotopic variations in granitic rocks. *Earth Planet. Sci. Lett.* **1988**, *90*, 263–271. [CrossRef]
101. Turner, S.; Foden, J.; Morrison, R. Derivation of some A-type magmas by fractionation of basaltic magma: An example from the Padthaway Ridge, South Australia. *Lithos* **1992**, *28*, 151–179. [CrossRef]
102. Winter, J.D. *Principles of Igneous and Metamorphic Petrology*; Pearson Education Limited: London, UK, 2014.
103. Bolhar, R.; Weaver, S.; Whitehouse, M.; Palin, J.; Woodhead, J.; Cole, J. Sources and evolution of arc magmas inferred from coupled O and Hf isotope systematics of plutonic zircons from the Cretaceous Separation Point Suite (New Zealand). *Earth Planet. Sci. Lett.* **2008**, *268*, 312–324. [CrossRef]
104. Barboni, M.; Schoene, B. Short eruption window revealed by absolute crystal growth rates in a granitic magma. *Nat. Geosci.* **2014**, *7*, 524–528. [CrossRef]
105. Li, S.M.; Wang, Q.; Zhu, D.C.; Stern, R.J.; Cawood, P.A.; Sui, Q.L.; Zhao, Z.D. One or Two Early Cretaceous Arc Systems in the Lhasa Terrane, Southern Tibet. *J. Geophys. Res. Solid Earth* **2018**, *123*, 3391–3413. [CrossRef]
106. Rapp, R.P.; Watson, E.B. Dehydration Melting of Metabasalt at 8–32 kbar: Implications for Continental Growth and Crust-Mantle Recycling. *J. Petrol.* **1995**, *36*, 891–931. [CrossRef]
107. Castillo, P.R.; Janney, P.E.; Solidum, R.U. Petrology and geochemistry of Camiguin Island, southern Philippines: Insights to the source of adakites and other lavas in a complex arc setting. *Contrib. Mineral. Pet.* **1999**, *134*, 33–51. [CrossRef]
108. Rogers, N.; Macdonald, R.; Fitton, J.; George, R.; Smith, M.; Barreiro, B. Two mantle plumes beneath the East African rift system: Sr, Nd and Pb isotope evidence from Kenya Rift basalts. *Earth Planet. Sci. Lett.* **2000**, *176*, 387–400. [CrossRef]
109. Xiong, X.L.; Liu, X.C.; Zhu, Z.M.; Li, Y.; Xiao, W.S.; Song, M.S.; Zhang, S.; Wu, J.H. Adakitic rocks and destruction of the North China Craton: Evidence from experimental petrology and geochemistry. *Sci. China Earth Sci.* **2011**, *54*, 858–870. [CrossRef]
110. Li, C.D.; Zhang, Q.; Miao, L.C.; Meng, X.F. Mesozoic high-Sr, low-Y and low-Sr, low-Y types granitoids in the northern Hebei Province: Geochemistry and petrogenesis and its relation to mineralization of gold deposits. *Acta Petrol. Sin.* **2004**, *20*, 269–284, (In Chinese with English Abstract).
111. Macpherson, C.G.; Dreher, S.T.; Thirwall, M.F. Adakites without slab melting: High pressure differentiation of island arc magma, Mindanao, the Philippines. *Earth Planet. Sci. Lett.* **2006**, *243*, 581–593. [CrossRef]

112. Karsli, O.; Dokuz, A.; Uysal, İ.; Aydin, F.; Kandemir, R.; Wijbrans, J. Generation of the Early Cenozoic adakitic volcanism by partial melting of mafic lower crust, Eastern Turkey: Implications for crustal thickening to delamination. *Lithos* **2010**, *114*, 109–120. [CrossRef]
113. Bea, F. Residence of REE, Y, Th and U in granites and crustal protoliths: Implications for the chemistry of crustal melts. *J. Petrol.* **1996**, *37*, 521–552. [CrossRef]
114. Li, X.K.; Li, C.; Sun, Z.M.; Wang, M. Origin and tectonic setting of the giant Duolong Cu–Au deposit, South Qiangtang Terrane, Tibet: Evidence from geochronology and geochemistry of Early Cretaceous intrusive rocks. *Ore Geol. Rev.* **2017**, *80*, 61–78. [CrossRef]
115. Davidson, J.; Turner, S.; Handley, H.; Macpherson, C.; Dosseto, A. Amphibole "sponge" in arc crust? *Geology* **2007**, *35*, 787–790. [CrossRef]
116. Bea, F.; Pereira, M.D.; Stroh, A. Mineral/leucosome trace-element partitioning in a peraluminous migmatite (a laser ablation-ICP-MS study). *Chem. Geol.* **1994**, *117*, 291–312. [CrossRef]
117. Li, Y.L.; Zhang, H.F.; Guo, J.H.; Li, C.F. Petrogenesis of the Huili Paleoproterozoic leucogranite in the Jiaobei Terrane of the North China Craton: A highly fractionated albite granite forced by K-feldspar fractionation. *Chem. Geol.* **2017**, *450*, 165–182. [CrossRef]
118. Xiang, Y.X.; Yang, J.H.; Chen, J.Y.; Zhang, Y. Petrogenesis of Lingshan highly fractionated granites in the Southeast China: Implication for Nb-Ta mineralization. *Ore Geol. Rev.* **2017**, *89*, 495–525. [CrossRef]
119. Li, S.; Guilmette, C.; Ding, L.; Xu, Q.; Fu, J.J.; Yue, Y.H. Provenance of Mesozoic clastic rocks within the Bangong-Nujiang suture zone, central Tibet: Implications for the age of the initial Lhasa-Qiangtang collision. *J. Asian Earth Sci.* **2017**, *147*, 469–484. [CrossRef]
120. Li, S.; Yin, C.Q.; Ding, L.; Guilmette, C.; Zhang, J.; Yue, Y.H.; Baral, U. Provenance of Lower Cretaceous sedimentary rocks in the northern margin of the Lhasa terrane, Tibet: Implications for the timing of the Lhasa-Qiangtang collision. *J. Asian Earth Sci.* **2020**, *190*, 104162. [CrossRef]
121. Basta, F.F.; Maurice, A.E.; Bakhit, B.R.; Azer, M.K.; El-Sobky, A.F. Intrusive rocks of the Wadi Hamad Area, North Eastern Desert, Egypt: Change of magma composition with maturity of Neoproterozoic continental island arc and the role of collisional plutonism in the differentiation of arc crust. *Lithos* **2017**, *288–289*, 248–263. [CrossRef]
122. Clemens, J.; Darbyshire, D.; Flinders, J. Sources of post-orogenic calcalkaline magmas: The Arrochar and Garabal Hill–Glen Fyne complexes, Scotland. *Lithos* **2009**, *112*, 524–542. [CrossRef]
123. Lee, C.T.A.; Morton, D.M.; Kistler, R.W.; Baird, A.K. Petrology and tectonics of Phanerozoic continent formation: From island arcs to accretion and continental arc magmatism. *Earth Planet. Sci. Lett.* **2007**, *263*, 370–387. [CrossRef]
124. Frost, C.D.; Swapp, S.M.; Frost, B.R.; Finley-Blasi, L.; Fitz-Gerald, D.B. Leucogranites of the Teton Range, Wyoming: A record of Archean collisional orogeny. *Geochim. Cosmochim. Acta* **2016**, *185*, 528–549. [CrossRef]
125. Kapp, P.; DeCelles, P.G.; Gehrels, G.E.; Heizler, M.; Ding, L. Geological records of the Lhasa-Qiangtang and Indo-Asian collisions in the Nima area of central Tibet. *GSA Bull.* **2007**, *119*, 917–933. [CrossRef]
126. Zhang, Q.H.; Ding, L.; Cai, F.L.; Xu, X.X.; Zhang, L.Y.; Xu, Q.; Willems, H. Early Cretaceous Gangdese retroarc foreland basin evolution in the Selin Co basin, central Tibet: Evidence from sedimentology and detrital zircon geochronology. *Geol. Soc. Lond. Speéc. Publ.* **2011**, *353*, 27–44. [CrossRef]
127. Zhu, Z.C.; Zhai, Q.G.; Hu, P.Y.; Tang, Y.; Wang, H.T.; Wang, W.; Wu, H.; Huang, Z.Q. Timing of the Lhasa–Qiangtang Collision: Constraints from the sedimentary records of the Duoni Formation from the middle segment of the Bangong–Nujiang suture zone. *Acta Sedimentol. Sin.* **2019**, *38*, 712–726, (In Chinese with English Abstract).
128. Lai, W.; Hu, X.M.; Garzanti, E.; Xu, Y.W.; Ma, A.L.; Li, W. Early Cretaceous sedimentary evolution of the northern Lhasa terrane and the timing of initial Lhasa-Qiangtang collision. *Gondwana Res.* **2019**, *73*, 136–152. [CrossRef]
129. Chen, Y.F.; Ding, L.; Li, Z.Y.; Laskowski, A.K.; Li, J.X.; Baral, U.; Qasim, M.; Yue, Y.H. Provenance analysis of Cretaceous peripheral foreland basin in central Tibet: Implications to precise timing on the initial Lhasa-Qiangtang collision. *Tectonophysics* **2020**, *775*, 228311. [CrossRef]
130. Sun, J.; Mao, J.W.; Beaudoin, G.; Duan, X.Z.; Yao, F.J.; Ouyang, H.G.; Wu, Y.; Li, Y.B.; Meng, X.Y. Geochronology and geochemistry of porphyritic intrusions in the Duolong porphyry and epithermal Cu-Au district, central Tibet: Implications for the genesis and exploration of porphyry copper deposits. *Ore Geol. Rev.* **2017**, *80*, 1004–1019. [CrossRef]
131. England, P.C.; Thompson, A.B. Pressure-temperature-time paths of regional metamorphism, part I: Heat transfer during the evolution of regions of thickened continental crust. *J. Petrol.* **1984**, *25*, 894–928. [CrossRef]
132. Bea, F. The sources of energy for crustal melting and the geochemistry of heat-producing elements. *Lithos* **2012**, *153*, 278–291. [CrossRef]
133. Xiao, B.; Li, Q.G.; Liu, S.W.; Wang, Z.Q.; Yang, P.T.; Chen, J.L.; Xu, X.Y. Highly fractionated Late Triassic I-type granites and related molybdenum mineralization in the Qinling orogenic belt: Geochemical and U–Pb–Hf and Re–Os isotope constraints. *Ore Geol. Rev.* **2014**, *56*, 220–233. [CrossRef]
134. Cao, H.W.; Li, G.M.; Zhang, R.Q.; Zhang, Y.H.; Zhang, L.K.; Dai, Z.W.; Zhang, Z.; Liang, W.; Dong, S.L.; Xia, X.B. Genesis of the Cuonadong tin polymetallic deposit in the Tethyan Himalaya: Evidence from geology, geochronology, fluid inclusions and multiple isotopes. *Gondwana Res.* **2021**, *92*, 72–101. [CrossRef]
135. Dilles, J.H.; Kent, A.J.R.; Wooden, J.L.; Tosdal, R.M.; Koleszar, A.; Lee, R.G.; Farmer, L.P. Zircon compositional evidence for sulfur-degassing from ore-forming arc magmas. *Econ. Geol.* **2015**, *110*, 241–251. [CrossRef]
136. Guo, C.L.; Zeng, L.S.; Gao, L.E.; Su, H.Z.; Ma, X.H.; Yin, B. Highly fractionated granitic minerals and whole-rock geochemistry prospecting markers in Hetian, Fujian Province. *Acta Geol. Sin.* **2017**, *91*, 1796–1817, (In Chinese with English Abstract).
137. Mohamadizadeh, M.; Mojtahedzadeh, S.H.; Ayati, F. Ga-(Nb+Ta)-(Nb/Ta)(Zr/Hf) Ternary Diagram: An Excellent Tool for Discriminating Barren and Ta-Hosting Granite-Pegmatite Systems. *J. Earth Sci.* **2020**, *31*, 551–558. [CrossRef]

138. Farahat, E.S.; Azer, M.K. Post-collisional magmatism in the northern Arabian-Nubian Shield: The geotectonic evolution of the alkaline suite at Gebel Tarbush area, south Sinai, Egypt. *Geochemistry* **2011**, *71*, 247–266. [CrossRef]
139. Ballouard, C.; Poujol, M.; Boulvais, P.; Branquet, Y.; Tartèse, R.; Vigneresse, J.L. Nb-Ta fractionation in peraluminous granites: A marker of the magmatic-hydrothermal transition. *Geology* **2016**, *44*, 231–234. [CrossRef]